

A&A manuscript no.
(will be inserted by hand later)

Your thesaurus codes are:
08.09.2; 09.01.1; 13.21.3

Detection of spatial variations in the (D/H) ratio in the local interstellar medium. ^{*}

Alfred Vidal-Madjar¹, Martin Lemoine², Roger Ferlet¹, Guillaume Hébrard¹, Detlev Koester³, Jean Audouze¹, Michel Cassé^{4,1}, Elisabeth Vangioni-Flam¹, and John Webb⁵

¹ Institut d'Astrophysique de Paris, CNRS, 98 bis boulevard Arago, 75014 Paris, France

² DARC, UPR-176 CNRS, Observatoire de Paris-Meudon, 92195 Meudon Cédex, France

³ Universitaet Kiel, Germany

⁴ CEA/DSM/DAPNIA, Service d'Astrophysique, Saclay, 91191 Gif-sur-Yvette, France

⁵ School of Physics, University of New South Wales, Sydney, NSW 2052, Australia

Received; accepted

Abstract. We present high resolution ($\Delta\lambda \simeq 3.7\text{km.s}^{-1}$) HST-GHRS observations of the DA white dwarf G191-B2B, and derive the interstellar D/H ratio on the line of sight. We have observed and analysed simultaneously the interstellar lines of H I, D I, N I, O I, Si II and Si III. We detect three absorbing clouds, and derive a total H I column density $N(\text{H I})=2.4\pm 0.1 \times 10^{18}\text{cm}^{-2}$, confirming our Cycle 1 estimate, but in disagreement with other previous measurements.

We derive an average D/H ratio over the three absorbing clouds $N(\text{D I})_{\text{total}}/N(\text{H I})_{\text{total}}=1.12\pm 0.08 \times 10^{-5}$, in disagreement with the previously reported value of the local D/H as reported by Linsky *et al.* (1995) toward Capella. We re-analyze the GHRS data of the Capella line of sight, and confirm their estimate, as we find $(\text{D/H})_{\text{Capella}} = 1.56 \pm 0.1 \times 10^{-5}$ in the Local Interstellar Cloud in which the solar system is embedded. This shows that the D/H ratio varies by at least $\sim 30\%$ within the local interstellar medium.

Furthermore, the Local Interstellar Cloud is also detected toward G191-B2B, and we show that the D/H ratio in this component, toward G191-B2B, can be made compatible with that derived toward Capella. However, this comes at the expense of a much smaller value for the D/H ratio as averaged over the other two components, of order 0.9×10^{-5} , and in such a way that the D/H ratio as averaged over all three components remains at the above value, *i.e.* $(\text{D/H})_{\text{Total}} = 1.12 \times 10^{-5}$.

We thus conclude that, either the D/H ratio varies from cloud to cloud, and/or the D/H ratio varies within the Local Interstellar Cloud, in which the Sun is embed-

ded, although our observations neither prove nor disprove this latter possibility.

Key words: Stars: Individual: G191-B2B – ISM: abundances – Ultraviolet: ISM

1. Introduction

Deuterium is only produced in primordial Big Bang nucleosynthesis (BBN), and destroyed in stellar interiors (Epstein, Lattimer & Schramm 1976). Hence, any abundance of deuterium measured at any metallicity should provide a lower limit to the primordial deuterium abundance (Reeves *et al.* 1972). Deuterium is thus a key element in cosmology and in galactic chemical evolution (*e.g.*, Steigman, Schramm & Gunn 1977; Audouze & Tinsley 1976; Vidal-Madjar & Gry 1984; Boesgaard & Steigman 1985; Olive *et al.* 1990; Vangioni-Flam & Cassé 1995; Prantzos 1996, Scully *et al.* 1997). The primordial abundance of deuterium is indeed the best probe of the baryonic density parameter of the Universe Ω_B , and the decrease of its abundance with galactic evolution traces, amongst other things, the amount of star formation.

The first, although indirect, measurement of the deuterium abundance of astrophysical significance was carried out through ³He in the solar wind, leading to $\text{D/H} \simeq 2.5 \pm 1.0 \times 10^{-5}$ (Geiss & Reeves 1972), a value representative of an epoch 4.5 Gyrs past. The first measurements of the interstellar D/H ratio, representative of the present epoch, were reported shortly thereafter (Rogerson & York 1973). Their value of $\text{D/H} \simeq 1.4 \pm 0.2 \times 10^{-5}$ has not changed ever since. The most accurate measurement of the interstellar D/H ratio was reported by Linsky *et al.* (1993, 1995, hereafter L93, L95) in the direction of Capella, using HST-GHRS, $\text{D/H} \simeq 1.6 \pm 0.1 \times 10^{-5}$ (statistical + systematic).

Send offprint requests to: A. Vidal-Madjar

^{*} Based on observations with the NASA/ESA Hubble Space Telescope, obtained at the Hubble Space Telescope Science Institute which is operated by the Association of Universities for Research in Astronomy Inc., under NASA contract NAS5-26555.

Up to a few years ago, these measurements were used to constrain BBN in a direct way. The situation has changed, as measurements of the D/H ratio in metal-deficient quasars absorbers, at moderate and high redshift, have become available (*e.g.*, Carswell *et al.* 1994; Songaila *et al.* 1994; Tytler, Fan & Burles 1996; Webb *et al.* 1997; Burles & Tytler 1998a,b; see also Burles & Tytler, 1998c for a review). However, these observations have not provided a single definite value of the primordial D/H ratio. At the present time, it is not known whether the higher estimates of the primordial D/H ratio reported are artifacts due to the mimicking of the D I line by an H I interloper, or whether the ratios reported (low or high) are discrepant due to errors in interpreting the velocity structure, or whether substantial fluctuations (a factor ~ 6) actually exist.

On similar grounds, it turns out that determinations of the interstellar D/H ratio do not generally agree on a single value, even in the very local medium (Vidal-Madjar *et al.* 1986, Murthy *et al.* 1987, 1990). For instance, $D/H < 10^{-5}$ is measured toward λ Sco (York, 1983), while in the opposite direction toward α Aur, $D/H = 1.65 \times 10^{-5}$ (L93, L95). On longer pathlengths, $D/H \simeq 7. \times 10^{-6}$ is measured toward δ and ϵ Ori (Laurent *et al.* 1979), and $D/H \simeq 5. \times 10^{-6}$ toward θ Car (Allen *et al.* 1992). Although several scenarios have been proposed to explain these putative variations (*e.g.*, Vidal-Madjar *et al.* 1978; Bruston *et al.* 1981), the above measurements are still unaccounted for. Despite the high quality of the data, it may nevertheless be possible that even better data is required to overcome systematic effects.

The only way to derive a reliable estimate of the interstellar D/H ratio is to observe the atomic transitions of D and H in the far-UV, in absorption in the local ISM against the background continuum of cool or hot stars. These observations have been performed using the Copernicus and IUE satellites, and now the Hubble Space Telescope. Both types of target stars present pros and cons.

The main advantage of observing cool stars is that they can be selected in the vicinity of the Sun. This results in low H I column densities, and simple lines of sight. A difficulty inherent to the cool stars approach is that the detailed structure of the line of sight can be obtained only through the observation of the Fe II and the Mg II ions, which are unfortunately not proper tracers of H I. In particular, species like N I and O I could not be observed. Moreover, the estimate of the H I column density always depends strongly on the modeling of the chromospheric Lyman α emission line. The Capella target of L93, L95 is a double system with two cool stars: it provided a line of sight with a single absorbing component (see however Sec.5), and allowed a very accurate estimate of the D/H ratio, as the emission line could be modeled by observing the binary system at different phases.

Hot stars are unfortunately located further away from the Sun, so that one always has to face a high H I column

density and often a non-trivial line of sight structure. In these cases, D I could not be detected at Ly α , and one has to observe higher order lines, *e.g.* Ly γ , Ly δ , Ly ϵ . The stellar continuum is however smooth at the location of the interstellar absorption and, moreover, the N I triplet at 1200 Å as well as other N I lines are available to probe the velocity structure of the line of sight. N I and O I were shown to be reliable tracers of H I in the ISM (Ferlet 1981; York *et al.* 1983).

We introduced in Cycle 1 of HST a new type of target, white dwarfs, which should solve many of the intrinsic difficulties of the problem. Indeed, such targets may be chosen in the high temperature range where the depth of the photospheric Lyman α line is reduced, so as to obtain a significant flux at the bottom of the H I stellar absorption line where the interstellar D I and H I lines appear, as well as a smooth stellar continuum. Also, these targets may be chosen close to the Sun so that the line of sight is not too complex. We observed in HST Cycle 1 the white dwarf G191-B2B, at medium resolution $\Delta\lambda \simeq 18\text{km.s}^{-1}$ (Lemoine *et al.* 1996).

We proceeded further in this approach with Cycle 5 high resolution ($\Delta\lambda \simeq 3.7\text{km.s}^{-1}$) Echelle-A data of H I, D I, as well as N I and O I, and Si II and Si III, in order to derive an accurate velocity and ionization structure of the line of sight. We present these new spectroscopic observations of the white dwarf G191-B2B in Section 2. In Section 3 we present the analysis of these data; the results are further analysed in Section 4. We re-analyze the Capella line of sight in Section 5, and summarize our conclusions in Section 6.

2. Observations and Data Reduction.

2.1. Observations

Our new observations of the white dwarf G191-B2B were performed with GHRS/HST in July 1995 (Cycle 5 Guest Observer proposal ID5893). The spectra were acquired in the wavelength ranges 1196–1203Å, 1200–1207Å, 1212–1219Å and 1299–1307Å using the Echelle-A grating. The log of these observations is presented in Table 1.

The Echelle-A grating provides a nominal resolving power of $\sim 80\,000$, or a spectral resolution of 3.7 km.s^{-1} . We used only the Small Science Aperture (SSA), corresponding to $0.25''$ on the sky and illuminating 1 diode to achieve the best possible resolving power. For further details on the instrumentation, see Duncan (1992).

G191-B2B is a DA spectral type white dwarf located 40-70 pc away from the Sun, with an effective temperature $T_{\text{eff}} = 61190 - 61700\text{K}$, gravity $\text{Log}(g) = 7.49 - 7.61$ (Finley *et al.* 1997; Vauclair *et al.* 1997), and magnitude $m_v = 11.8$, as determined from optical data fitted with pure hydrogen models. It fulfills all the criteria for a good candidate to measure the D/H ratio. Apart from D I and H I at Lyman α , we obtained the spectra of the lines N I(1199Å, 1200Å,

Table 1. List of lines observed in 1995 during Cycle 5 at high spectral resolution $\Delta\lambda \simeq 3.5\text{km.s}^{-1}$.

File	Element	Central Wave. (Å)	Observing Date (1995)	Grating	Exp. Time (s)	S/N
z2q30208m	H I, D I	1215.45	Jul 26, 22:18	ECH-A	6528	21
z2q3020ct	H I, D I	1215.45	Jul 27, 00:59	ECH-A	6528	21
z2q3020gt	H I, D I	1215.45	Jul 27, 03:39	ECH-A	6528	21
z2q30108t	N I	1199.94	Jul 26, 13:30	ECH-A	4896	25
z2q3010dt	N I, Si III	1203.57	Jul 26, 18:27	ECH-A	3917	19
z2q3010cm	O I, Si II	1303.01	Jul 26, 16:31	ECH-A	4570	26

1201Å), Si III(1206Å), O I(1302Å) and Si II(1304Å) using Echelle-A. The observation at high spectral resolution of O I and N I should allow us to resolve possible different H I absorbing clouds on the line of sight, while the observation of Si II and Si III should allow the detection of possible H II gas. From the comparison of the b values of different atomic weights, an estimate of the temperature and turbulent velocity in the different clouds is also possible, while the analysis of the Si II and Si III lines should determine the ionization structure of the line of sight. In particular, the observed lines of N I, Si II and Si III are not saturated, and should therefore provide accurate estimates of the column densities. The O I 1302Å line is slightly saturated in this low H I column density environment, and should thus offer a reasonable estimate of the column densities, as well as of the b -values. At the end, we expect to obtain a sufficient number of constraints on all parameters involved in the analysis of the Lyman α lines of D I and H I, but the D/H ratios of the different components.

2.2. Data reduction.

Our data were reduced with the Image Reduction and Analysis Facility (IRAF) software, using the STSDAS package. During the observations, we used the FP-SPLIT mode which splits the total exposure time into successive cycles of 4 sub-exposures, each corresponding to a slightly different projection of the spectrum on the photocathode. We used the “quarter stepping” mode, which provides a sample of 4 pixels per resolution element. This oversamples the spectrum (since for instance the SSA does not fulfill the Nyquist sampling criterion), and allows to correct for the granularity of the photocathode. Indeed, the effect of the photocathode on each diode being the same for the four sub-exposures, it is possible to evaluate this granularity from the comparison of the 4 sub-exposures where a constant granularity effect mixes with a non-constant photon statistical noise.

We found that the standard method for correcting for the granularity, which is available in the IRAF-STSDAS package, was not efficient as a result of the impact of the geomagnetic field on the photocathode. The geomagnetic field deflects the incident electron beam on the diodes in a way depending on the location of the HST on its orbit,

thus making the granularity pattern non-constant from sub-exposure to sub-exposure. As a result, the standard iterative method leads to the appearance of noisy features whose intensity increases with the number of iterations. We therefore developed a different procedure based on the use of simple statistical filters.

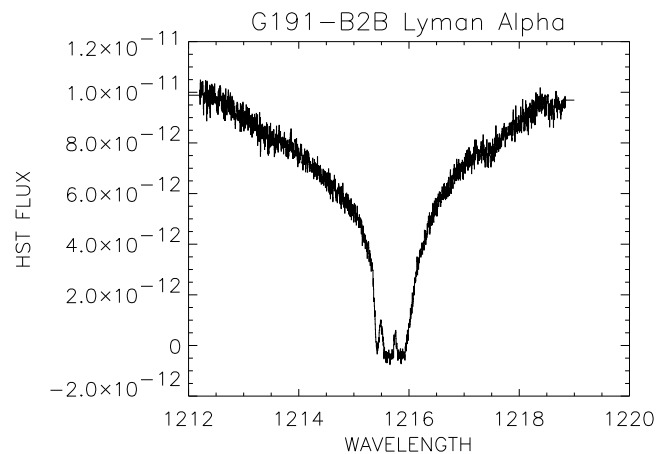


Fig. 1. Data taken with the Echelle-A in the Lyman α region. Some perturbations due to the photocathode inhomogeneities can be seen near 1213.4 and 1217.5 Å. Note the deuterium absorption at 1215.3Å. The central peak at the bottom of the saturated H I Lyman α line corresponds to the earth geocoronal emission. Note also that the bottom of the saturated Lyman α line is not at exact zero level.

We first cross-correlate the different spectra corresponding to the same spectral ranges, *i.e.* the different sub-exposures of a same exposure, and shift them accordingly so that real absorption or emission features correspond to the same pixel values in each spectrum. We next compute the median and the standard deviation with respect to that median at each pixel, our statistical sample being the set of intensities of the different spectra at that pixel. Finally, we compute the average intensity value at each pixel, rejecting the intensities of the different spectra deviating from the median by more than, say, 3 standard deviations. We found that this simple treatment resulted

in good signal-to-noise ratios (Fig. 1) while avoiding any residual ghost feature (see Bertin *et al.* 1995 for more details).

We chose to rebin our spectra to two pixels per diode in all cases but O I, *i.e.* two pixels per resolution element approximately, which is the standard sampling mode, using the IRAF-STSDAS procedure. In the case of O I the very sharp edges of the line contain most of the information, and we thus decided to keep four pixels per resolution element so as to take advantage of the oversampling available in these observations.

In the case of Lyman α , the spectral signature is not as sharp, and, moreover, the S/N ratio is significantly lower at the bottom of the line, and we thus developed a second approach to check the consistency of our procedure. We re-align the sub-exposures using the deuterium line, which is clearly detected in each of the sub-exposure, as a reference. This procedure means we are unable to correct for the photocathode granularity. Nonetheless, it appears that no such defect is present at Lyman α . In effect, such defects are of order $\sim 10\%$, and are thus easily detected when adding the sub-exposures corresponding to *a priori* the same spectral instrument shift, thereby improving the S/N ratio and building four different shifted spectra where the photocathode defects appear at fixed positions. This process allowed us to show that the amplitude of photocathode defects in the Lyman α central region does not exceed a few percent. One clearly sees such defects in Fig. 1 in the far wings of the Lyman α profile, around 1213.4Å and 1217.5Å (these defects were not perfectly corrected through the first approach). Thus the final Lyman α line profile is well represented in the region from 1213.6Å to 1217.3Å, and the region that we use in our data analysis is even further reduced to 1214.5-1217.0Å, where the spectral information lies.

As a second consistency check, we measure the width of the geocoronal emission line. Spurious shifts in the co-adding procedure would degrade the spectral resolution. The geocoronal emission line should be a very narrow feature, only slightly broader than the nominal instrument spectral resolution. We find, fitting the emission line with a gaussian, an equivalent Doppler width $b \simeq 5.7\text{km.s}^{-1}$, corresponding to a temperature $T \simeq 1950\text{K}$, after deconvolution from the instrumental profile. At this point, one should note that the geocorona fills up the SSA, so that its width results from the convolution of the intrinsic width with the spectrograph instrumental profile, and with the profile of a point source broadened by the projection of the SSA on the spectral scale; this latter effect amounts to broadening the SSA instrumental profile by 4 pixels. The above measured width thus corresponds to an intrinsic temperature $T \sim 600\text{K}$, which is a very plausible average value for the Earth exosphere temperature. We note that this consistency test is all the more significant as the geocoronal emission line only shows up in the final co-added sub-exposures. Therefore, the procedure used

for co-addition produces a sharp line profile in which the Echelle-A spectral resolution is kept at its highest nominal value.

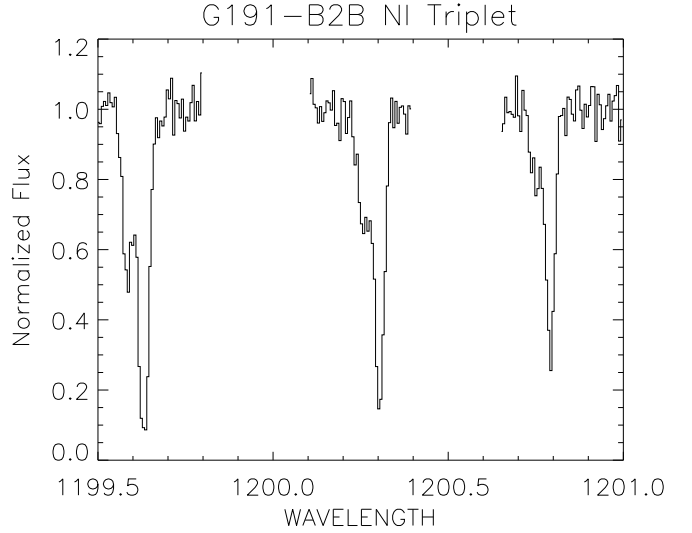


Fig. 2. The normalized N I triplet data used in the fitting procedure.

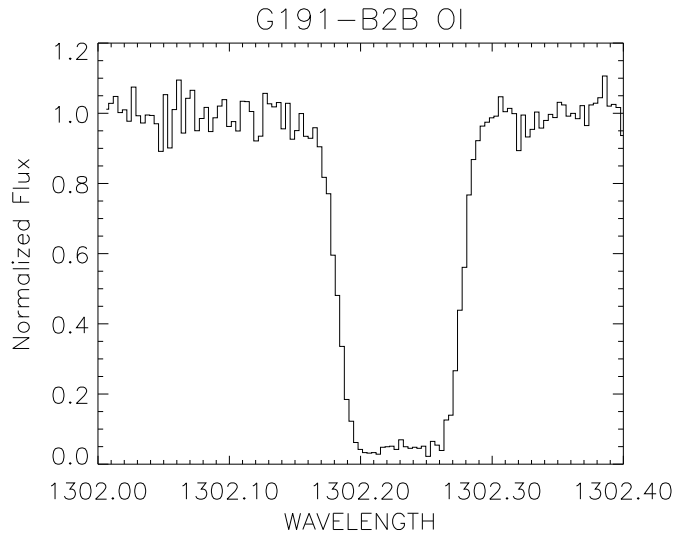


Fig. 3. Same as Fig. 2. The O I line.

Each exposure was preceded by a special platinum lamp calibration which allowed us to calculate the residual shift left by the standard CAL-HRS calibration procedure. Together with the oversampling mode, this correction allowed us to reach an absolute calibration accuracy of $\pm 1.5\text{km.s}^{-1}$ in radial velocity. Hereafter, the radial velocities will be given in the heliocentric rest frame.

The different spectral lines were normalized to a continuum of unity by a polynomial whose degree, typically

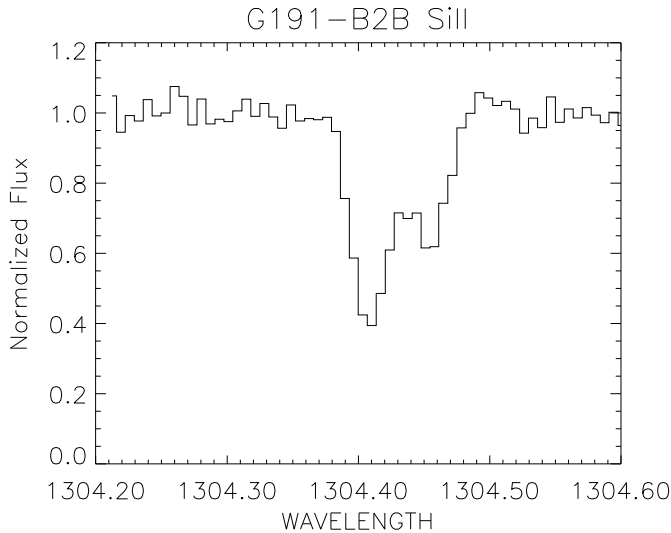


Fig. 4. Same as Fig. 2. The Si II line.

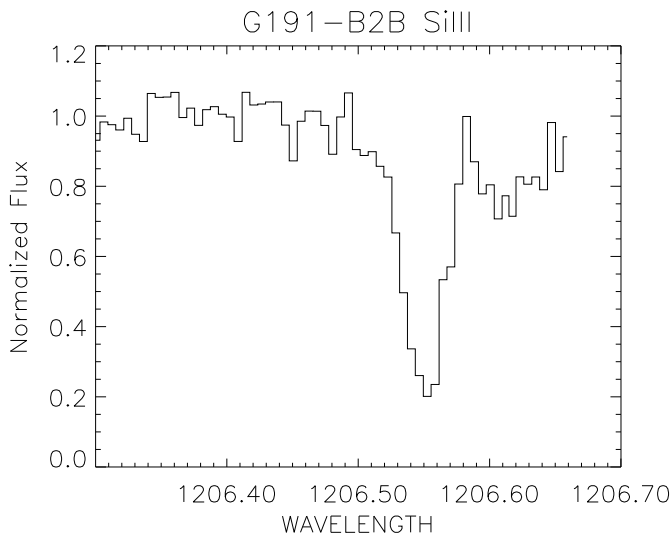


Fig. 5. Same as Fig. 2. The Si III line. Note that the broad line on the red side is of photospheric origin (see text).

2 – 7, was chosen according to a cross-validation statistical procedure. The normalized spectra are shown in Fig. 2, Fig. 3, Fig. 4 and Fig. 5. Since the continuum level is determined to high precision, we do not need to take into account any continuum fitting parameters in the line fitting. The Lyman α line was not normalized in this way, as the stellar continuum is a Lorentzian profile, with a deep core; the stellar continuum at Lyman α is described at length later.

Finally, in the case of the Si III line (1206Å), we decided to keep in the spectrum the nearby signature of the photospheric Si III stellar line on the red wing of the interstellar Si III line (see Fig. 5). This photospheric line was thus fitted along with the interstellar features as an additional component. This gave access to an independent

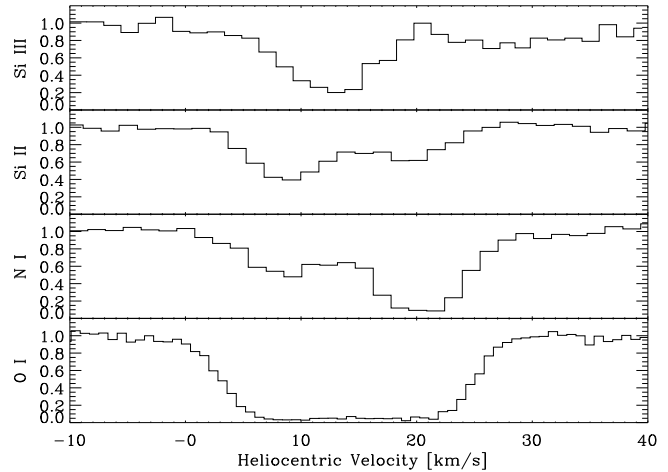


Fig. 6. The absorption features seen in different species, as indicated on the left hand side of the figure, superposed in velocity space. Two obvious components are seen in Si II and N I. A third component in between the other two is detected in the Si III and O I lines. The two components at the shortest wavelengths, seen in Si III, are H II regions, while the component at ~ 20 km s $^{-1}$ is the Local Cloud, an H I region. It is obvious that deducing velocity structure of lines of sight for D/H evaluations from ionized species could be extremely misleading.

evaluation of the intrinsic shift of the white dwarf photospheric features, a parameter that is also involved in our final analysis of the deuterium and hydrogen Lyman α profiles.

2.3. The number of absorption components along the line of sight

We first evaluate the number of components present on the line of sight. This number represents a minimum number of components since blends are always possible.

Figure 6 illustrates all species (excluding H I and D I) observed with the Echelle-A spectrograph. It is clear, from the N I and Si II profiles, that at least two clearly resolved components are present. In the Si III line, the strongest component falls in between the other two seen in N I and Si II. This cannot be due to an incorrect absolute calibration of one of the spectral ranges, as we observed the Si III line at 1206Å together with the N I line at 1201Å in the same exposure. The relative shift between these two species, from one end of the detector to the other, should certainly be less than 0.5 km.s $^{-1}$. This Si III component is thus real, and obviously more ionized than the other two.

A broad component is also detected in Si III at the edge of the observed spectral range. When fitted with a single absorption feature, assuming that the broadening is thermal, the corresponding temperature is of order 30000 K, *i.e.* much broader than clouds usually seen in the local ISM. Because its heliocentric velocity is $\simeq 29$ km.s $^{-1}$, it is

reasonable to assume that this line is of photospheric origin. Indeed, as shown in Vidal-Madjar *et al.* (1994), photospheric features in G191-B2B are relatively broad and their observed heliocentric velocities are $\sim 35 \pm 4 \text{ km.s}^{-1}$. Predictions of the strength of the Si III photospheric line are also in agreement with the observations. We thus do not include this feature in our study.

The O I profile confirms, through profile fitting, the need for a third interstellar component, located in between the two components seen in N I and Si II. The O I signature of this third component is mainly the flatness of the absorption in the saturated core. We also note that there is no component around 29 km.s^{-1} in the other lines, consistent with the photospheric interpretation of the broad Si III feature.

2.4. The residual flux at the bottom of the spectral lines.

In order to properly evaluate the strength of the different ISM components contributing to the observed absorption, it is extremely important to evaluate the level of the zero flux which may be slightly erroneous in an echelle spectrograph, due to the diffuse light produced from the adjacent spectral orders. The case of Lyman α is obvious as the broad saturated core allows us to accurately determine for the zero level. We corrected the Lyman α region for this zero level by subtracting the flux in the Lyman α core from the whole line profile. Correcting for the zero level in the GHRS data reduction pipeline is indeed difficult for other species, as it depends on instrumental parameters as well as on the (unknown) spectrum shape in adjacent orders. Thus, for species other than H I, we determined the zero level as the best fit value, *i.e.* the one corresponding to a minimum χ^2 , of all O I, N I, Si II, and Si III lines fitted simultaneously. In each χ^2 calculation as a function of the zero level, the same zero level value was adopted for the O I and Si II lines, and for the N I and Si III lines, since these pairs were observed in the same sub-exposures. In each case, only the O I and N I lines contributed significantly to determining the zero level values, as the lines of Si II and Si III are too weak. The N I lines are sensitive to the zero level as the strongest line is almost saturated, and because these lines form a triplet and their measured relative strengths depend on the zero level. For our data normalized to unity, the value and the error bar of the N I and Si III zero levels is: 0.038 ± 0.02 , *i.e.* consistent with zero level within the accuracy of our measurement. Since the O I line is saturated, the zero level position is sharply defined. The measured value of the zero level, for both O I and Si II lines, is: 0.032 ± 0.004 . These values will be used from now on in our analysis and their impact on the evaluated parameters will be considered as minor in the forthcoming study and checked in few specific cases.

3. The total H I and D I content

3.1. The stellar Lyman Alpha profile

It is well known that the limiting factor of an accurate D/H ratio measurement is generally the measurement of the H I column density itself, as the D I line at Lyman α is not saturated for $N(\text{H I}) \sim 10^{18} \text{ cm}^{-2}$. In the present case, $N(\text{H I})$ can be measured with good accuracy from the damping wings of the H I Lyman α profile. However, we first need to model the stellar continuum, as the Lorentzian shape of the intrinsic Lyman α photospheric line may mimic interstellar damping wings, and affect the $N(\text{H I})$ measurement. We thus calculated Lyman α profiles from LTE atmosphere models using the appropriate stellar parameters. Another LTE profile, as well as NLTE calculations, both using codes completely different from ours, were kindly provided by Stefan Dreizler. A qualitative difference between these profiles is that LTE profiles are not as sharp and deep as NLTE profiles.

In our analysis, the different possible continua were considered (see Fig. 7) in order to evaluate the possible systematic error one could make on the total H I evaluation.

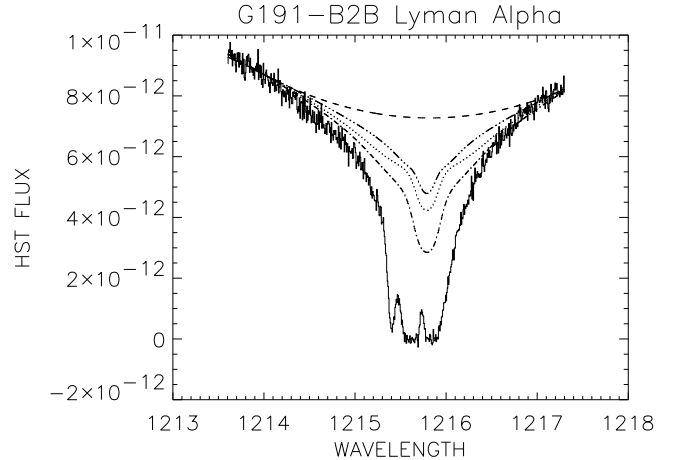


Fig. 7. The different calculated Lyman α photospheric continua assumed in our analysis: from top to bottom, a simple 2nd order polynomial, a first LTE calculation (DK), a second LTE calculation (S. Dreizler, private communication) and an NLTE calculation (S. Dreizler, private communication). These three latter profiles were shifted by 29 km.s^{-1} to match the measured radial velocity of G191-B2B.

The heliocentric radial velocity of G191-B2B photospheric lines (including gravitational redshift) is known to be $24 \pm 5 \text{ km.s}^{-1}$ from ground based observations (Reid and Wegner 1988). From our Cycle 1 observations, we measured a differential velocity $\simeq 35 \pm 4 \text{ km.s}^{-1}$ compared to the nearby interstellar lines (Vidal-Madjar *et al.* 1994); this shift was however evaluated from medium resolution data in which the ISM components were not resolved.

In the present high resolution Echelle-A data, the photospheric Si III line falls at a radial velocity $29 \pm 1.5 \text{ km.s}^{-1}$. This line is however located at the end of our spectral range, and the profile shape may be partially distorted, inducing a shift in the measured velocity. We also tentatively identified six Fe V and six Ni V photospheric lines in the 1300–1306 Å region, whose average location gives a radial velocity $24.8 \pm 4.0 \text{ km.s}^{-1}$. All these measurements are in good agreement, and their weighted least square average results in a radial velocity (including gravitational redshift): $28.9 \pm 1.3 \text{ km.s}^{-1}$. With a gravitational redshift of order $\sim 25 \text{ km.s}^{-1}$ (Finley *et al.* 1997), the radial velocity of G191-B2B itself is thus of order $\sim 5 \text{ km.s}^{-1}$ a typical value for an object in the local galactic environment.

With this information, we produced different data sets for the Lyman α line, each corresponding to the normalization of the observed data by a theoretical stellar continuum. From now on, we fix the radial velocity of the stellar profile at 29 km.s^{-1} . Finally, we defined an additional “Lyman α photospheric profile” with a second order polynomial, in order to circumvent any assumption made about the shape of the profile itself. This polynomial continuum is derived by fitting to the far wings of the interstellar line in the ranges 1213.6–1213.9 Å and 1217.0–1217.3 Å (see Fig. 7). In fact, we found that the best solution (minimum χ^2) was obtained for this second order polynomial further corrected by a fourth order polynomial in the core of the line, the latter being fitted together with the interstellar Lyman α line.

We now have four different profiles, hence four normalized data sets. From these, we discard the stellar profile corresponding to the LTE calculation of S. Dreizler, since, as shown in Fig. 7, this profile is intermediate between our LTE calculation, and the NLTE calculation of S. Dreizler. We thus keep these two latter extreme case, plus the second order polynomial. Hereafter, we respectively denote these continua as LTE29, NLTE29, and 2nd Polynomial.

3.2. The total H I and D I column densities

We now evaluate the total column densities of H I and D I along the line of sight. We make different assumptions about the stellar continuum as well as the number of components along the line of sight, in order to evaluate their impact on the estimate of the column densities. Namely, for each of the above three stellar continua, we assume a further correction to the continuum, given either by a first order polynomial, or a fourth order polynomial; in each case, these further corrections are fitted simultaneously with the physical parameters of the line of sight. As to the number of components on the line of sight, we performed the calculation for one, two, three, and four interstellar components. We certainly know from the other elements that there are at least three absorbing components; what we want to show here, however, is that the evaluation of the total column densities, and hence the

Table 2. Reduced χ^2 (with 349 degrees of freedom) and several parameters corresponding to the Lyman α fits with the 3 different assumed stellar profiles: 2nd order polynomial, LTE29 and NLTE29 (see text). Only the H I and D I lines were fitted, with all parameters free (see text), and only **one** component on the line of sight. The order of the polynomial adjusted on top of the reconstructed stellar continuum is indicated, either 1st order or 4th order.

1 st order polynomial fit			
Stellar cont.	2 nd Pol.	LTE29	NLTE29
χ^2	1.91	1.51	2.52
$N(\text{H I})_{\text{Tot}} \text{ (cm}^{-2}\text{)}$	3.00×10^{18}	2.21×10^{18}	1.80×10^{18}
$N(\text{D I})_{\text{Tot}} \text{ (cm}^{-2}\text{)}$	2.43×10^{13}	2.51×10^{13}	2.66×10^{13}
$(\text{D/H})_{\text{Tot}} \text{ (}\times 10^5\text{)}$	0.81	1.14	1.48
4 th order polynomial fit			
Stellar cont.	2 nd Pol.	LTE29	NLTE29
χ^2	1.13	1.51	2.02
$N(\text{H I})_{\text{Tot}} \text{ (cm}^{-2}\text{)}$	2.32×10^{18}	2.21×10^{18}	2.00×10^{18}
$N(\text{D I})_{\text{Tot}} \text{ (cm}^{-2}\text{)}$	2.60×10^{13}	2.66×10^{13}	2.66×10^{13}
$(\text{D/H})_{\text{Tot}} \text{ (}\times 10^5\text{)}$	1.12	1.20	1.33

Table 3. Same as Table 2 but with **three** components on the line of sight. All three components are required to present a unique D/H value. Here, the total D/H ratio represents the ratio of the total D I column density to the total H I column density.

1 st order polynomial fit			
Stellar cont.	2 nd Pol.	LTE29	NLTE29
χ^2	1.83	1.33	2.05
$N(\text{H I})_{\text{Tot}} \text{ (cm}^{-2}\text{)}$	2.92×10^{18}	2.12×10^{18}	1.70×10^{18}
$N(\text{D I})_{\text{Tot}} \text{ (cm}^{-2}\text{)}$	2.58×10^{13}	2.70×10^{13}	2.93×10^{13}
$(\text{D/H})_{\text{Tot}} \text{ (}\times 10^5\text{)}$	0.88	1.27	1.72
4 th order polynomial fit			
Stellar cont.	2 nd Pol.	LTE29	NLTE29
χ^2	1.03	1.32	1.71
$N(\text{H I})_{\text{Tot}} \text{ (cm}^{-2}\text{)}$	2.38×10^{18}	2.01×10^{18}	1.92×10^{18}
$N(\text{D I})_{\text{Tot}} \text{ (cm}^{-2}\text{)}$	2.73×10^{13}	2.73×10^{13}	2.79×10^{13}
$(\text{D/H})_{\text{Tot}} \text{ (}\times 10^5\text{)}$	1.15	1.30	1.45

average D/H ratio, are not sensitive to the number of components. Finally, in order to further show the strength of this prediction, we do not take into account any physical constraint coming from other species, *i.e.* O I, N I, Si II, or Si III. When those elements are included in a global fit of the line of sight, this will narrow down the margin of freedom for the D/H ratios.

The results of some of the parameters of these fits are presented in Table 2, for a one cloud solution, and in Table 3 for three absorbing components. The results are similar for a two component structure of the line of sight. Several comments can be made at this stage. We note that the theoretical continua have very well defined shapes, with abrupt features in their profile at various points near the core. When the interstellar absorption is superimposed, mismatches could be introduced in the re-

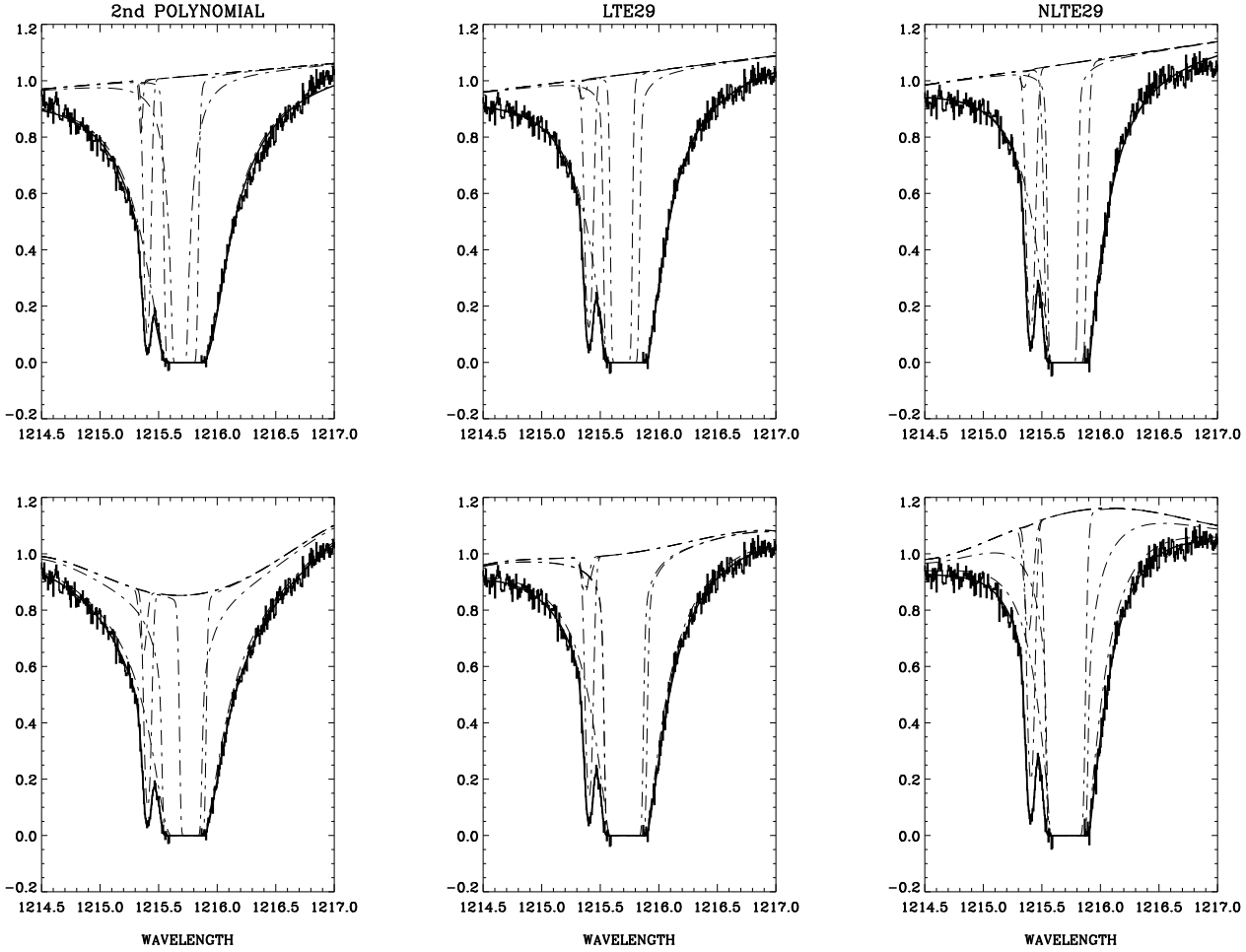


Fig. 8. The different fits are presented for the Lyman α line when several stellar continua are assumed. The upper panels correspond to a 1st order polynomial fit on top of the assumed stellar continuum, while the lower panels correspond to a 4th order polynomial fit. From left to right the panels correspond to the three stellar continua presented here, *i.e.* 2ndPolynomial, LTE29 and NLTE29 (see text). The central panels show that the LTE29 profile is probably a good approximation to the real stellar photospheric profile, since the 4th order polynomial fit does not improve the fit with respect to the 1st order polynomial. On the contrary, the 2ndPolynomial is not deep enough in the core, while the NLTE29 is too deep. Once corrected for their erroneous shape, the solutions found in terms of total H I and total D/H are similar (see Table 3). The χ^2 values favor the 2nd \times 4th stellar continuum (see text).

sulting final profile. However, as shown in Fig. 8, the 4th order correction deepens the 2nd order polynomial in the core of the line to mimic a Lorentzian profile, but hardly modifies the LTE29 continuum. This means that the $\Delta\chi^2$, of order 100, in favor of the 2nd order continuum, is mostly intrinsic to the LTE29 profile.

The above fits also reveal that LTE continua are generally favored (in terms of χ^2) when compared to NLTE continua. This is illustrated by the fact that a 4th order correction plus the NLTE profile tends to the LTE continuum (see Fig. 8). One could be surprised by this result, since NLTE model atmospheres should be more appropriate than LTE calculations at the high temperature of G191-B2B. That the LTE profiles seem to fit better may partly be due to the fact that we compare pure hydrogen

models only. G191-B2B is well-known to contain significant amounts of heavy metals, which are visible in high-resolution UV spectra and which even completely dominate the EUV spectrum (*e.g.*, Wolff *et al.* 1998). Taking into account the blanketing effect of these metals leads to a decrease of the effective temperature by about 5000 K, and may also lead to a better agreement of NLTE profiles with the observations. These details are, however, inconsequential for the present study.

In summary, these χ^2 analyses give two main results: the 2nd \times 4th order polynomial is largely favored over the theoretical continua; it is also supported by the absolute χ^2 value, with a reduced χ^2 close to unity. We can thus conclude that this continuum offers a very good approximation to the actual stellar continuum of G191-B2B, and

we adopt this for our determination of the (D/H) ratio. When we include all other species in the profile fitting, we obtain the same result, namely that the 2nd × 4th order polynomial continuum is very largely favored over the other theoretical continua. Although all subsequent profile fittings were also carried out for these continua, we will not refer to them any more. Finally, we also checked that the presence of more than 3 components on the line of sight does not change these results. Indeed, repeating the same procedure with 4 components led to results that are nearly identical to those of the 3 cloud solution, in terms of total H I and D I column densities.

Given these considerations, we study the relative variation of the χ^2 as a function of the total D/H ratio, in order to derive confidence intervals on this quantity, according to the so-called $\Delta\chi^2$ method. Strictly speaking, this method is exact for gaussian quantities, and, more generally, correct up to second order in the variation of the parameters. The 2σ confidence level around a given parameter should then be reached when the χ^2 of the fit with the parameter fixed to this $\pm 2\sigma$ value becomes equal to $\chi_0^2 + 4$, where χ_0^2 is the total best-fit χ^2 with the parameter left as free. The 3σ level is obtained for $\chi_0^2 + 9$, *etc.* However, this assumes that the quantities are gaussian, that the data points (pixel values) are uncorrelated, and that their error bars are accurately known. We prefer to relax these assumptions, and set the threshold for an “effective” 2σ level at $\chi_0^2 + 10$. This provides a *very* conservative and *very* safe range of errors. In particular, we note that this procedure has the great advantage of including in the error bars so-derived all errors on other parameters that would have to be propagated and projected on the parameter under study. In effect, when looking for a χ^2 value for a given value of the parameter, away from the best fit value, the profile fitting tends to accommodate the values of the other parameters so as to obtain the smallest χ^2 hence the smallest $\Delta\chi^2$. This is especially important when different parameters are strongly correlated, *e.g.* column densities anti-correlated with broadening parameters, or column densities correlated with other column densities. However, we note that, strictly speaking, this method can only be applied to statistical errors, and not to systematic errors, which tend to add linearly, rather than quadratically. Since this method is CPU time expensive, we only use to determine error bars on D/H ratios. For other quantities, that do not constitute our primary concern, we will quote error bars estimates obtained through trial and error.

Here, from the variations of the χ^2 as a function of the D/H ratio, we obtain, for three components, and a unique D/H ratio:

$$(D/H)_{\text{Total}} = 1.15 \pm 0.1 \times 10^{-5}.$$

In the above, uncertainties arising from the choice of the stellar continuum are included in the quoted error bars, because of the simultaneous fitted 4th order correction to the continuum. However, systematic errors, that

could arise from uncertain calibration, or physics left out of our model, are not included.

4. The component by component analysis

4.1. The components velocity separation and column density ratios

No information on the velocity structure of the line of sight can be obtained from Lyman α as the components have too large intrinsic widths in D I and H I to be resolved. Therefore, we now turn to a detailed analysis of the other species, O I, N I, Si II, and Si III, to extract the required information.

In order to do so, we perform a fit of all lines of O I, N I, Si II, and Si III, simultaneously, assuming three components on the line of sight. This means, more precisely, that we define one velocity, one temperature, and one turbulent broadening for each cloud; the column densities of the various species are also free parameters. The absorption profile corresponding to these physical parameters is then computed for each absorber and for each absorption line, and the total profile is compared to the observations. We then minimize the sum of the total χ^2 of each absorption line. The best fit values of the physical parameters is presented in Table 4. In this table, most of the error bars are tentative, obtained by trial and error, *i.e.* they represent a rough estimate of the actual error bar; this is however sufficient for our present purpose.

Among these physical parameters, the radial velocities and the column densities are the best determined, as would be expected. The temperature and turbulent broadening are indeed slightly degenerate as the mass separation between these species is insufficient. We note that the radial velocities are determined to a high degree of confidence in the spectral regions where they are resolved, *e.g.* Si III for component 2, and N I, O I, and Si II for components 1 and 3, due to the large number of sampling points on the profile. (We recall that the components are numbered from 1 to 3 in order of increasing radial velocity). The error on the estimate of their radial velocity is dominated, in a given spectral region, by the calibration accuracy $\pm 1.5 \text{ km.s}^{-1}$. When averaged over all spectral regions, the accuracy should thus be of order $\pm 0.8 \text{ km.s}^{-1}$. The relative shifts in radial velocity between the various components are not affected by the absolute calibration accuracy; their error bars are however of order $\pm 0.5 \text{ km.s}^{-1}$ but will be greatly improved later. We obtained these error bars by performing fits to all species but one, each species being excluded in turn, and averaging the resulting radial velocities and their shifts.

It is especially important to note the radial velocity of the third component, $V = 20.3 \pm 0.8 \text{ km.s}^{-1}$. This component is identified with the Local Interstellar Cloud (LIC) in which the Sun is embedded (*e.g.*, Lallement & Bertin 1992; Bertin *et al.* 1995). This cloud has been detected in

Table 4. The ISM components characteristics in the direction of G191-B2B as evaluated from the O I, N I, Si II and Si III lines (from the blue to the red the components are noted 1, 2 and 3; component 3 is identified with the LIC and noted as such). The error bars are estimated from the different fits produced, *i.e.* fits with all the lines and with all the lines but one included. Note that the error bars on components 1 and 2 are in some cases larger simply because these two components are blended. As well, note that the values given here will change slightly when the H I and D I lines are included in the profile fitting, see subsequent tables.

	Component 1	Component 2	LIC
V (km.s ⁻¹)	8.2 ± 0.8	13.2 ± 0.8	20.3 ± 0.8
T (K)	8000. ± 4000.	8000. ± 6000.	7000. ± 4000.
σ (km.s ⁻¹)	1.5 ± 1.5	2.5 ± 1.5	1.2 ± 1.2
N(O I) (cm ⁻²)	2.8 ± 1.0 × 10 ¹⁴	1.5 ± 1.0 × 10 ¹⁴	3.1 ± 0.5 × 10 ¹⁴
N(N I) (cm ⁻²)	1.2 ± 0.3 × 10 ¹³	3.5 ± 1.0 × 10 ¹²	6.7 ± 0.4 × 10 ¹³
N(Si II) (cm ⁻²)	1.9 ± 0.3 × 10 ¹³	8.4 ± 4.0 × 10 ¹²	1.1 ± 0.2 × 10 ¹³
N(Si III) (cm ⁻²)	4.0 ± 3.0 × 10 ¹¹	2.2 ± 0.5 × 10 ¹²	< 10 ¹¹

the direction of nearly all nearby stars, and its velocity vector relative to the Solar System was found to be:

$$V_{\text{LIC}} = 25.7 \text{ km.s}^{-1}$$

$$l_{II}(\text{LIC}) = 186.1^\circ$$

$$b_{II}(\text{LIC}) = -16.4^\circ.$$

This component is actually the only absorbing cloud detected toward Capella, whose line of sight is only separated by $\simeq 7^\circ$ from the G191-B2B line of sight. The projections of the LIC velocity on the Capella and G191-B2B lines of sight are respectively 21.96 km.s^{-1} , and 20.26 km.s^{-1} . We therefore obtain a radial velocity in excellent agreement with the prediction. This value is of importance as it allows us to check the consistency of our approach: we expect to detect this component, and we know its predicted velocity within the calibration internal error $\pm 0.8 \text{ km.s}^{-1}$. Taking into account the appearance of the LIC in four spectral domains (D I, O I, N I, and Si II), we conclude that we actually well detected and correctly identified it with component 3. From now on, we thus refer to this component as the LIC.

Finally, we note that the column density ratios between the components are relatively close to 1. This is illustrated in the following Table (from the blue to the red the components are noted 1, 2 and LIC; component 1 is used as the reference):

Components N ratios	2/1	LIC/1
O I	0.5	1.1
N I	0.3	5.6
Si II	0.4	0.6
Si III	5.5	< 0.02

This also provides another consistency check. Namely, when a solution is obtained for H I and D I, the column density ratios between the different components should remain close to the values obtained for O I, and/or N I. As far as N I, Si II, and Si III are concerned, the error on these ratios, and in particular the LIC to 1 ratio, is expected to be relatively small, $\lesssim 40\%$, as the lines are not

saturated. Notably, this implies that the various components have very different ionization structures. Obviously, components 1 and 2 are more ionized than the LIC. Interestingly enough, O I and N I do not appear to behave similarly; this trend will be confirmed below, where a more detailed analysis is performed including H I and D I.

4.2. The H I and D I content of each component

We now turn to the final analysis, *i.e.* all observed lines fitted simultaneously. We recall that our fitting procedure works in terms of absorbing components, so that a unique set of radial velocity, temperature and turbulent broadening is used to calculate all absorption profiles of all lines for a given component. These physical parameters are thus fitted simultaneously over the lines of D I, H I, O I, N I, Si II, and Si III; we assume the presence of three components on the line of sight. The total number of degrees of freedom available is ~ 800 .

The best fit, without including any extra constraint on the parameter space, is shown for the Lyman α line in Fig. 9, and is enlarged around the D I line in Fig. 10. This best fit is obtained for a 2nd × 4th order continuum, and the reduced χ^2 is $\chi^2 = 1.12$ for 795 degrees of freedom. We note that the physical parameters obtained, given in Table 5, are in good agreement with those obtained from the fits of the O I, N I, Si II, and Si III lines only. Moreover, the individual χ^2 corresponding to each spectral region, derived here from a simultaneous fit of all lines, are close to those obtained for individual fits of each spectral region. This supports the idea that the structure of the line of sight is well determined. Finally, we find column density ratios between components, in H I and in D I, that lie relatively close to those obtained for O I and N I in the previous fit of O I, N I, Si II, and Si III, as well as in this global fit. That our results indicate that H I, D I, O I, and N I behave in a similar way, represents a strong consistency check. Indeed, it is well known that these four elements have very similar ionization properties, and, in particular, that they are locked by charge exchange in a typical ISM

Table 5. Reduced χ^2 , $\Delta\chi^2$ (total) and several parameters corresponding to the fits made with the different constraints assumed. All observed lines are included in the profile fitting, and all parameters are free, except otherwise noted in boldface. The first column gives the best-fit all parameters free result; the subsequent columns give results for various constraints: respectively, for a unique D/H ratio between the three components, for a unique N(O I)/N(H I) ratio, for a unique N(N I)/N(H I) ratio, for a D/H ratio in the LIC corresponding to that found by L93, L95, and, finally, for the LIC D/H ratio, temperature and turbulent broadening corresponding to those found by L93, L95, toward Capella. In all cases, the stellar continuum is a 2nd \times 4th order polynomial.

Constraint	free	H I follows D I	H I follows O I	H I follows N I	(D/H) _{LIC}	(D/H,T, σ) _{LIC}
χ^2_{Tot}	1.12	1.12	1.13	1.17	1.12	1.15
$\Delta\chi^2_{\text{Tot}}$	0.0	3.9	14.6	41.8	5.8	25.6
$\chi^2_{\text{Lyman } \alpha}$	1.04	1.05	1.06	1.14	1.05	1.07
N(H I) _{Tot} ($\times 10^{-18}$) (cm ⁻²)	2.39	2.42	2.33	2.09	2.43	2.37
N(D I) _{Tot} ($\times 10^{-13}$) (cm ⁻²)	2.68	2.63	2.68	2.99	2.69	2.71
(D/H) _{Tot} ($\times 10^5$)	1.12	1.09	1.15	1.43	1.11	1.14
V ₁ (km.s ⁻¹)	8.18	8.21	8.12	8.27	8.30	8.25
T ₁ (K)	11160.	11027.	10040.	12573.	11213.	11453.
σ_1 (km.s ⁻¹)	0.25	0.63	1.16	0.10	0.63	0.18
N(H I) ₁ ($\times 10^{-18}$) (cm ⁻²)	0.310	0.277	0.728	0.325	0.220	0.210
N(D I) ₁ ($\times 10^{-13}$) (cm ⁻²)	0.535	0.301	0.477	0.658	0.523	0.477
(D/H) ₁ ($\times 10^5$)	1.73	1.09	0.66	2.02	2.38	2.27
V ₂ (km.s ⁻¹)	13.21	13.28	13.28	13.30	13.44	13.36
T ₂ (K)	2575.	5150.	3200.	2650.	2925.	3475.
σ_2 (km.s ⁻¹)	3.12	2.76	3.04	3.08	2.84	2.92
N(H I) ₂ ($\times 10^{-18}$) (cm ⁻²)	1.08	1.27	0.430	0.103	1.52	1.42
N(D I) ₂ ($\times 10^{-13}$) (cm ⁻²)	1.05	1.38	1.10	0.912	1.07	1.05
(D/H) ₂ ($\times 10^5$)	0.97	1.09	2.56	8.85	0.70	0.74
V _{LIC} (km.s ⁻¹)	20.36	20.35	20.36	20.32	20.34	20.30
T _{LIC} (K)	4160.	3627.	5707.	7467.	4373.	7000.
σ_{LIC} (km.s ⁻¹)	2.01	2.19	1.26	0.80	1.96	1.60
N(H I) _{LIC} ($\times 10^{-18}$) (cm ⁻²)	1.00	0.870	1.17	1.66	0.690	0.740
N(D I) _{LIC} ($\times 10^{-13}$) (cm ⁻²)	1.10	0.940	1.10	1.42	1.10	1.18
(D/H) _{LIC} ($\times 10^5$)	1.10	1.09	0.94	0.86	1.60	1.60
$\Delta V_{2-1} - \Delta V_{3-1}$ (km.s ⁻¹)	5.03-12.18	5.07-12.14	5.16-12.24	5.03-12.05	5.14-12.04	5.11-12.05
H I ratio 2/1-3/1	3.48-3.22	4.58-3.14	0.59-1.61	0.32-5.11	6.91-3.14	6.76-3.52
D I ratio 2/1-3/1	1.96-2.06	4.58-3.14	2.31-2.31	1.39-2.16	2.05-2.10	2.20-2.47
O I ratio 2/1-3/1	0.57-1.12	0.56-1.10	0.59-1.61	0.56-1.26	0.49-1.10	0.52-0.91
N I ratio 2/1-3/1	0.41-5.61	0.40-5.61	0.46-5.84	0.32-5.11	0.34-5.37	0.31-5.13
Si II ratio 2/1-3/1	0.44-0.52	0.41-0.51	0.45-0.50	0.41-0.50	0.37-0.50	0.40-0.51
Si III ratio 2/1	5.73	4.99	5.35	4.99	4.25	4.77

environment. Provided that these elements have a unique abundance on the line of sight, one should therefore expect the abundance ratios of their neutrals to be unique.

We now go one step further with this idea, and test whether these elements can actually afford a unique neutral abundance on the line of sight. We thus require, in turn, the ratios N(D I)/N(H I), N(O I)/N(H I), and N(N I)/N(H I) to be unique (*i.e.*, equal from component to component), and the unique abundance kept as a free parameter, all other parameters as equally free as above, and we compare the χ^2 of these three solutions with the above best-fit χ^2 . The results are given in Table 5. Obviously, D I can be considered as a perfect tracer of H I on this line of sight, as the relative χ^2 difference with the above best fit is reasonably small, $\Delta\chi^2 = 3.9$. Two remarks are in order here. This result means that, within the quality of our data set, we do not detect variations of the D/H

ratio, from cloud to cloud; it does not mean either that we rule out such variations. Furthermore, that D I seems to trace H I holds here because we only consider one line of sight. When we compare the value for the D/H ratio measured here toward G191-B2B, with that measured toward Capella, in the next section, we will find that they disagree, and thus argue that the D/H ratio varies within the local ISM.

For O I, the situation is not as clear, as the χ^2 difference is larger, $\Delta\chi^2 = 14.6$. However, we note that in this profile fitting, the instrumental zero-level of the O I line was kept fixed (for numerical reasons). The O I line is saturated, and the column density ratios between components in O I thus depend on the value of the zero-level. If one were to incorporate this additional freedom on the value of the zero-level (within its error bars), the relative χ^2 difference would decrease. Therefore we do not feel that the above

$\Delta\chi^2$ rules out O I as a tracer of H I. In the case of N I, however, our results indicate that it cannot be considered as a perfect tracer of H I, as the χ^2 difference is quite large, $\Delta\chi^2 = 41.8$. Varying the zero-level for the N I lines cannot account for this large $\Delta\chi^2$, and we cannot find any other explanation than an actual difference in behavior between N I and the other neutrals D I, O I, and H I.

Finally, we wish to point out another important consistency check: whether we require D I or O I to be a tracer of H I, we obtain the same average D/H ratio. This supports the robustness of our measurement of the D/H ratio.

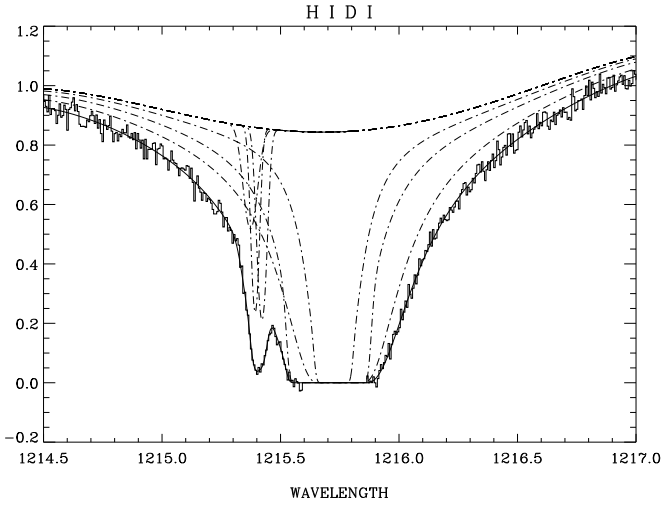


Fig. 9. The final fit for the H I and D I lines when all lines are taken into account and all parameters free.

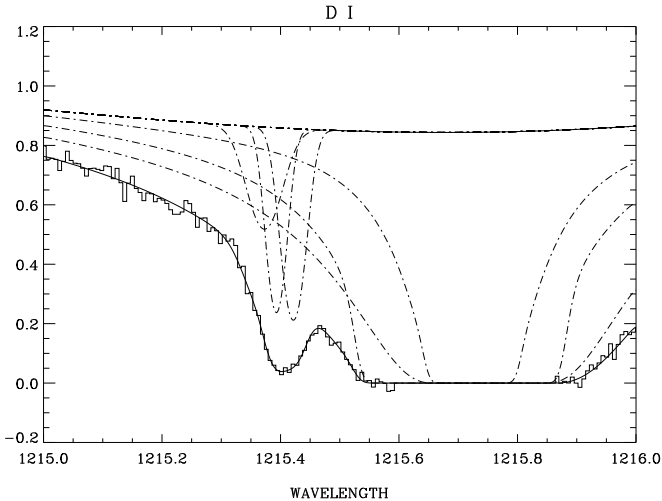


Fig. 10. The final fit enlarged over the D I line when all lines are taken into account and all parameters free.

We derived the error bar on the D/H ratio by studying the relative variation of the χ^2 as a function of the (unique) D/H ratio, as in section 3.2. This variation is

shown in Fig. 11, where we also plot the 2σ error bars estimates corresponding to a $\Delta\chi^2 = 10$ in the upper plot, together with the variation of the total H I and D I column densities in the lower panel. We finally obtain the following column densities and D/H ratio with an “effective” 1σ D/H error bar:

$$\begin{aligned} N(\text{H I})_{\text{Total}} &= 2.4 \pm 0.1 \times 10^{18} \text{cm}^{-2} \\ N(\text{D I})_{\text{Total}} &= 2.68 \pm 0.05 \times 10^{13} \text{cm}^{-2} \\ (\text{D/H})_{\text{Total}} &= 1.12 \pm 0.08 \times 10^{-5}, \end{aligned}$$

(the error bars for $N(\text{H I})$ and $N(\text{D I})$ are derived by trial and error; they are thus more tentative estimates but consistent with the D/H error bar).

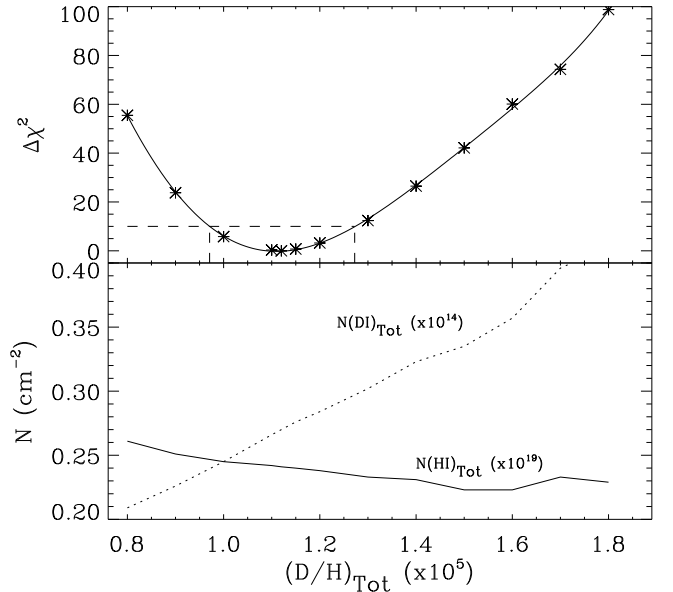


Fig. 11. Upper panel: relative χ^2 difference with respect to the best fit plotted *vs.* the D/H ratio. A unique D/H ratio was assumed on the line of sight. A spline was fitted to the numerical results, represented by stars. The dashed lines give the minimum and maximum value of the D/H ratio that correspond to $\Delta\chi^2 = 10$, or, according to our conventions, to an effective 2σ confidence interval. Lower panel: variation of the total H I and D I column densities *vs.* the D/H ratio, as indicated.

Let us now try two further hypotheses on this global line fitting. As we discussed in the previous section, component 3 is identified as the LIC, *i.e.* the interstellar cloud in which the Solar System is embedded. This component is also the unique component detected by L93, L95, toward Capella. Clearly, our average D/H ratio disagrees with their estimate of the D/H ratio toward Capella, in the LIC: $(\text{D/H}) = 1.6 \pm 0.1 \times 10^{-5}$. We now wish to see whether our D/H ratio in component 3, the LIC, can be reconciled with this latter value, and thus proceed to profile fitting, using $(\text{D/H}) = 1.6 \times 10^{-5}$ in the LIC component. As shown in Table 5, this solution is indeed com-

Table 6. Physical characteristics of the ISM components, numbered from 1 to 3 in the order of increasing radial velocity; component 3 is identified as the LIC, and noted as such. Here the accuracy on the velocities are relative. Absolute accuracy on the heliocentric velocities are of the order of 0.8km.s^{-1} . Error bars are tentative 1σ estimates, obtained by trial and error.

Component	1	2	LIC
V (km.s ⁻¹)	8.20 ± 0.20	13.20 ± 0.20	20.35 ± 0.05
T (K)	$11000. \pm 2000.$	$3000. \pm 2000.$	$4000._{-1500.}^{+2000.}$
σ (km.s ⁻¹)	0.5 ± 0.5	3.0 ± 0.5	$2.0_{-1.0.}^{+0.5.}$

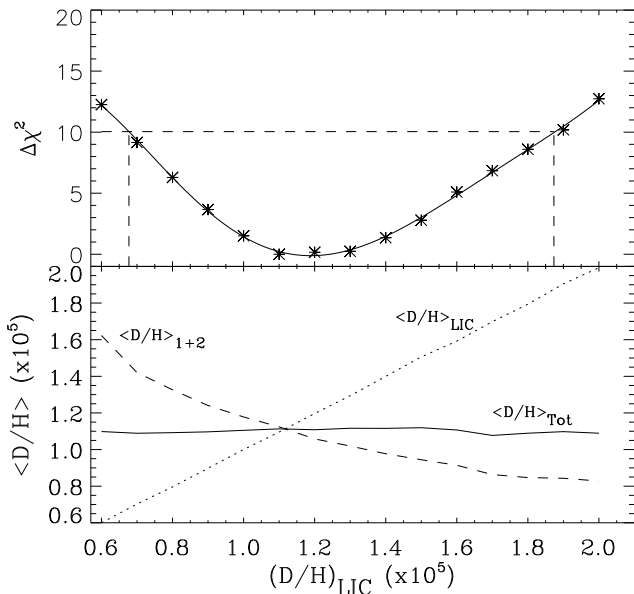


Fig. 12. Same as Fig. 11, except the D/H ratio varied is the LIC D/H. In the lower panel are plotted, as indicated, the evolution of the LIC D/H, the D/H averaged over components 1 and 2, and the total D/H averaged over components 1, 2, and LIC.

patible with our data set, as the relative χ^2 difference is reasonable, $\Delta\chi^2 = 5.8$. Obviously, such a high D/H ratio is permitted in the LIC because all three components on the line of sight to G191-B2B are thoroughly blended in the D I line. It also means that estimates of the D/H ratio in a particular component in our dataset is meaningless, as the D/H ratios between the three components are strongly correlated. This effect is shown in Figure 12, where we plotted the $\Delta\chi^2$, the D/H ratio averaged over components 1 and 2, and the total D/H *vs.* the LIC D/H. Indeed, the error bars on the LIC D/H ratio, that correspond (at 2σ , according to our conventions) to $\Delta\chi^2 = 10$, are rather large. However, it is quite interesting to note that the D/H ratio of the LIC, and that averaged over components 1 and 2, are anti-correlated. This translates itself in that the total D/H ratio remains constant when the LIC D/H ratio is varied from 0.6×10^{-5} to 2.0×10^{-5} . We obtain the following column densities in the LIC along

with the corresponding D/H ratio with an “effective” 1σ D/H error bar:

$$\begin{aligned} N(\text{H I})_{\text{LIC}} &= 1.0 \pm 0.3 \times 10^{18} \text{cm}^{-2} \\ N(\text{D I})_{\text{LIC}} &= 1.1 \pm 0.1 \times 10^{13} \text{cm}^{-2} \\ (\text{D/H})_{\text{LIC}} &= 1.19_{-0.25}^{+0.35} \times 10^{-5} \end{aligned}$$

(again, the error bars for $N(\text{H I})$ and $N(\text{D I})$ are derived by trial and error; they are thus more tentative estimates but consistent with the D/H error bar).

Finally, if we try to impose all characteristics of the LIC found by L93, L95, toward Capella, in our solution, we obtain $\Delta\chi^2=25.6$, which seemingly rules out this hypothesis. As we just showed that the LIC D/H ratio was compatible between the two line of sights, we are forced to conclude that there must be a significant difference in the line broadening of the LIC between both lines of sight (see however Section 5).

Let us therefore conclude on this study, as far as H I and D I are concerned. We find that performing a global fit on the line of sight gives good agreement with the individual fits performed on each spectral region. The average D/H ratio is tightly constrained to $\text{D/H}=1.12 \pm 0.08 \times 10^{-5}$. We also found that D I and O I are very reliable tracers of H I within the quality of our data; this is not the case for N I. Moreover, whether D I or O I are set as tracers of H I, *i.e.* a single column density ratio to H I is required on all three components, then the same average D/H ratio is obtained. This constitutes a strong consistency check of our results. Our average D/H ratio is in strong disagreement with that obtained by L93, L95 toward Capella. The D/H ratio in the LIC, which is the interstellar cloud common to both lines of sight, can be reconciled with the D/H found toward Capella. However, this comes at the expense of a significantly smaller D/H ratio in our components 1 and 2, of order 0.9×10^{-5} , while the D/H ratio averaged all three components remains the same, $(\text{D/H})_{\text{Total}} = 1.12 \times 10^{-5}$.

4.3. Results for each spectral line

We now briefly comment on the final solutions for the lines of O I, N I, Si II, and Si III, as obtained from the previous global fit of all lines including H I and D I. These results are summarized in Table 7.

Components 1 and 2 are blended in all observed lines, and therefore, individual results for either one of these two

Table 7. Column densities derived in the best-fit solution, obtained simultaneously on all lines and all species. The third and fifth column, respectively noted as “1+2”, and “Total”, give quantities averaged over components 1 and 2, and averaged over all three components, respectively. These are the most reliable quantities, as components 1 and 2 are blended in all observed lines. Error bars are tentative estimates, obtained by trial and error. Abundances are normalized to 10^6 hydrogen atoms.

Component	1	2	1+2	LIC	Total
N(O I) (cm^{-2})	2.6×10^{14}	1.5×10^{14}	4.0×10^{14}	$2.9 \pm 0.3 \times 10^{14}$	$6.9 \pm 0.3 \times 10^{14}$
N(O I)/N(H I) ($\times 10^6$)	823	135	288	287_{-80}^{+170}	288 ± 25
N(N I) (cm^{-2})	1.1×10^{13}	4.6×10^{12}	1.6×10^{13}	$6.3 \pm 0.4 \times 10^{13}$	$7.9 \pm 0.2 \times 10^{13}$
N(N I)/N(H I) ($\times 10^6$)	36	4	11	63_{-18}^{+33}	33 ± 2
N(Si II) (cm^{-2})	1.9×10^{13}	8.4×10^{12}	2.7×10^{13}	$1.0 \pm 0.1 \times 10^{13}$	$3.7 \pm 0.1 \times 10^{13}$
N(Si II)/N(H I) ($\times 10^6$)	62	8	20	10_{-3}^{+6}	16 ± 1
N(Si III) (cm^{-2})	3.9×10^{11}	2.2×10^{12}	2.6×10^{12}	$< 1.0 \times 10^{11}$	$2.6 \pm 0.2 \times 10^{12}$
N(Si III)/N(H I) ($\times 10^6$)	1.3	2.1	1.9	< 0.1	1.1 ± 0.1
N(Si II+Si III) (cm^{-2})	1.9×10^{13}	1.1×10^{13}	3.0×10^{13}	$1.0 \pm 0.1 \times 10^{13}$	$4.0 \pm 0.1 \times 10^{13}$
N(Si II+Si III)/N(H I) ($\times 10^6$)	63	10	22	10_{-3}^{+6}	17 ± 1
N(Si III)/N(Si II)	0.020	0.267	0.096	< 0.001	0.070

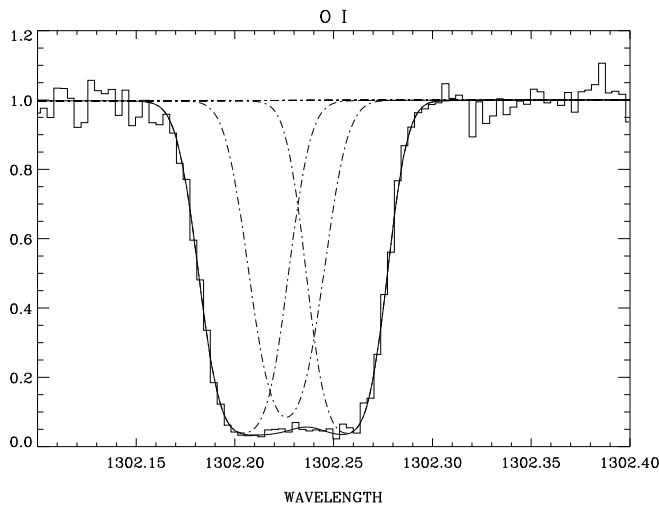


Fig. 13. The final fit for the O I line when all lines are taken into account and all parameters free.

components cannot be relied upon. We therefore discuss quantities averaged over these two components, and refer to them as ‘1+2’. The LIC characteristics are obtained with reasonable accuracy, while total column densities averaged over the line of sight are always the most accurate.

O I 1302Å:

The fit is shown in Fig. 13. The reduced χ^2 is 0.88 for 144 degrees of freedom, *i.e.* the fit is excellent.

The total abundance of O I (normalized to 10^6 hydrogen atoms) is $N(\text{O I})/N(\text{H I})=288 \pm 25$, almost identical to that found for the LIC. This value is also compatible with the average ISM gas neutral oxygen abundance, given by Meyer *et al.* (1998a): $N(\text{O I})/N(\text{H I})=319 \pm 14$. Meyer *et al.* (1998a) also evaluated that the average ISM (*gas+dust*) should be of the order of 500 assuming all O I atoms have returned to the gas phase. For comparison the solar value

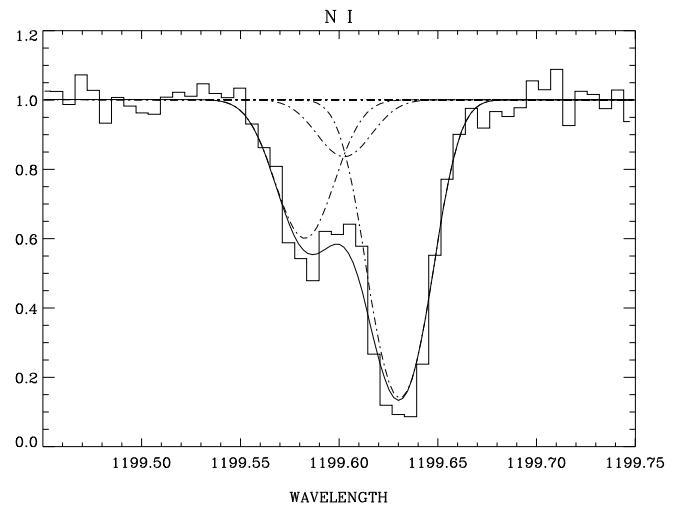


Fig. 14. The final fit for one of the N I lines of the triplet when all lines are taken into account and all parameters free.

is $N(\text{O I})/N(\text{H I})=741 \pm 130$ (Grevesse and Noels, 1993), different enough to lead these authors to conclude that the solar value may be enriched in oxygen. From Table 7, we see that the LIC appears as a normal diffuse interstellar cloud, as far as O I is concerned, just as the average of components 1 and 2. Our observations thus support the analysis of Meyer *et al.* (1998a), with some possible indication that component 1 has even returned all its O I to the gas phase.

N I 1200Å, triplet:

The fit for the strongest line of the triplet is shown in Fig. 14, and the total fit over the triplet gives a reduced χ^2 per degree of freedom (185) of 1.29. It is certainly less satisfactory than the O I fit; this seems to result from a slight mismatch between the three N I lines. Possibly, this may be due to some blending with weak photospheric lines

of other species (*e.g.*, FeV, NiV, ...). However, if a fit of the triplet is performed independently of all other lines, the solution is found to be very similar. We thus remain confident in the robustness of the N I results.

Ferlet (1981) found a strong relationship between N(H I) and N(N I) in a diffuse H I medium, on longer pathlengths, which translates for 10^6 hydrogen atoms to $N(\text{N I})/N(\text{H I})=62^{+45}_{-34}$. More recently, Meyer *et al.* (1998b) reached the following value for the N I interstellar abundance: $N(\text{N I})/N(\text{H I})=75 \pm 4$. These evaluations are compatible with the solar value of Grevesse & Noels (1993): $N(\text{N I})/N(\text{H I})=93 \pm 16$. We obtain, as an average over the line of sight, $N(\text{N I})/N(\text{H I})=33 \pm 2$, in agreement with our previous Cycle 1 observations (Lemoine *et al.* 1996) which gave a value of the order of 32, but significantly different from both the solar and ISM values. Interestingly, this difference seems to result from components 1 and 2, since their average value is $\simeq 11$. Furthermore the LIC nitrogen abundance seems to be compatible with the standard ISM values: $N(\text{N I})/N(\text{H I})=63^{+33}_{-18}$. As we discuss below, components 1 and 2 appear more ionized than the LIC; this would then suggest that the value of the N I/H I ratio is ionization dependent, and could further explain why N I does not turn out to be as reliable a tracer of H I as O I and D I were found to be.

Si II 1304Å:

The fit is shown in Fig. 15. The χ^2 per degree of freedom (72) is here equal to 0.98 and is thus again highly satisfactory.

We find similar column density ratios in Si II, Mg II, and Fe II. These two latter spectral regions were observed in Cycle 1 at medium and high resolution (Lemoine *et al.* 1996). The correspondence with these previous observations is as follows: components 1 and 2 are blended at medium and high resolution, and correspond to component A in Lemoine *et al.* (1996), while, similarly, component 3 corresponds to component B. The detection of a component C was reported in these previous observations, but it is not confirmed here. It probably was a ghost due to the wings of the pre-COSTAR GHRS Echelle-B point spread function. As Si II, Fe II, and Mg II have similar ionization properties up to first ionized level, the similarity of their column density ratios in each component certainly supports our results. We discuss below the ionization and depletion of the three components.

Si III 1206Å:

The fit is shown in Fig. 16. The χ^2 per degree of freedom (76) is 1.21 and is thus less satisfactory. However, this line falls at the end of the spectral range where the S/N ratio in the continuum varies strongly from pixel to pixel. We did not incorporate this instrumental effect in our profile fitting procedure. In effect, we adopted a unique S/N ratio for the whole continuum (calculated as the average over all pixels in the continuum), and derived error bars

for all pixels using this value of the S/N ratio in the continuum, weighted by the flux of the pixel, and combined quadratically with the background noise. Therefore, the variation of the S/N ratio in the continuum, from pixel to pixel, renders our χ^2 analysis less meaningful in this case. In any case, this line contributes to at most 10% of the total degrees of freedom (over all lines), so this cannot affect our global fit.

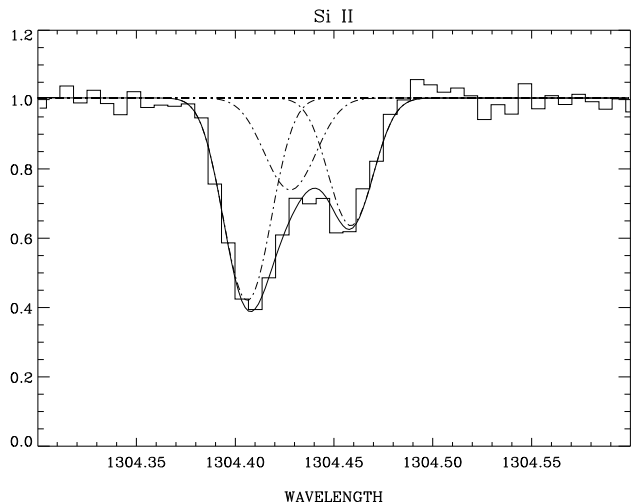


Fig. 15. The final fit for the Si II line when all lines are taken into account and all parameters free.

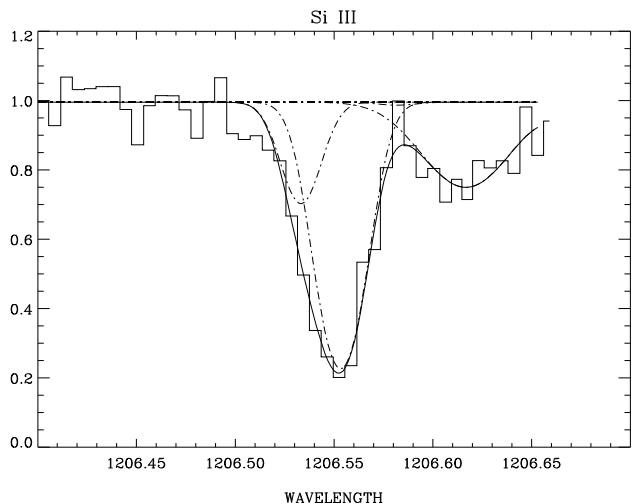


Fig. 16. The final fit for the Si III line when all lines are taken into account and all parameters free. The broad line on the red side is the photospheric Si III line observed at a 29km.s^{-1} heliocentric velocity. The LIC contribution to this line is negligible.

We confirm the average $N(\text{Si III})/N(\text{Si II}) \sim 10\%$ found in Lemoine *et al.* (1996). The three components have very different $N(\text{Si III})/N(\text{Si II})$ ratios. Components 1 and 2 are

more typical of HII regions, while the LIC is typical of an HI region. The ionization structure of components 1 and 2 is, however, non trivial. A $N(\text{Si III})/N(\text{Si II}) \sim 0.27$ ratio would indicate a significantly ionized region, yet the total broadening (thermal plus turbulent) of the line does not confirm this idea. Indeed, component 1 shows a high temperature ~ 11000 K and a low microturbulence $\sim 0.5 \text{ km.s}^{-1}$, whereas component 2 shows the opposite, namely, a low temperature ~ 3000 K, and a high microturbulence $\sim 3.0 \text{ km.s}^{-1}$. These two components may however constitute different parts of a shocked structure, with a velocity separation of $\sim 5.0 \text{ km.s}^{-1}$ as projected on the G191-B2B line of sight. This will be discussed somewhere else.

It is interesting to note that the $N(\text{Si III})/N(\text{Si II})$ ratio of the LIC has also been evaluated by Gry & Dupin (1998) in the direction of ϵ CMa. They found $N(\text{Si III})/N(\text{Si II}) \sim 0.41$, a very different result indeed. If confirmed, this difference may either show that the ionization structure within the LIC is inhomogeneous, or that the LIC may be confused by coincidence with another ISM component on the long ϵ CMa line of sight. More observations are needed to clarify this point.

On the basis of a simple model that calculates the ionization equilibrium between Si II and Si III (Dupin and Gry 1998), and assuming $n(\text{H II})=n_e$, we converted the Si III/Si II ratios listed in Table 7 into hydrogen ionization ratios, $N(\text{H II})/N(\text{H I})$, using the most recent value of $n(\text{H I}) \sim 0.24 \text{ cm}^{-3}$ (Puyoo & BenJaffel 1998). The derived value are respectively ~ 0.4 , ~ 0.5 , and $\lesssim 0.1$, for components 1, 2, and the LIC corresponding to $n_e \sim 0.12$, ~ 0.14 , and $\lesssim 0.03 \text{ cm}^{-3}$. Apparently, this estimate of the electron density of the LIC is much lower than a measurement obtained toward Capella using the ground and excited state lines of C II (Wood & Linsky 1997): $n_e = 0.11_{-0.06}^{+0.12} \text{ cm}^{-3}$. This discrepancy could be explained by arguing that the ionization in the LIC is far out of equilibrium, due for example to a shock ionizing event, which would tend to enhance the current electron density (Lyu & Bruhweiler 1996).

We can also use silicon to probe the degree of depletion in the three components, as it is more sensitive than oxygen or nitrogen. We find a total nitrogen to neutral hydrogen ratio averaged over the three components of ~ 17 , *i.e.* a factor two smaller than the cosmic value, $\simeq 35$ (per 10^6 hydrogen atoms). Therefore, provided the ionization of hydrogen is small, as our calculations seem to indicate, depletion remains relatively weak. This conclusion can be seemingly applied to the three components individually, or at least for 1+2 and the LIC, as inspection of Table 7 reveals. This low depletion is similar to the one observed in hot ISM clouds or in the galactic halo (see *e.g.* Spitzer and Fitzpatrick, 1993, 1995; Fitzpatrick and Spitzer, 1994, 1997; Jenkins and Wallerstein, 1996; Savage and Sembach, 1996) as well as in the so called ‘‘Cma tunnel’’ (Gry *et al.*, 1995; Dupin and Gry, 1998).

The comparison between the measured radial velocities of the components and the systemic radial velocity of G191-B2B, $v_{\text{G191-B2B}} = 5 \pm 2 \text{ km.s}^{-1}$, shows that none of these clouds seems to be associated with the star. In particular, the association of any of these clouds with an expansion shell centered on the star is precluded as the clouds have larger radial velocities than G191-B2B. A detailed discussion of the physical properties is clearly beyond the scope of the present work. This will be the subject of a forthcoming paper.

We derive a total HI column density of $N(\text{H I})=2.4 \pm 0.1 \times 10^{18} \text{ cm}^{-2}$, and confirm the previous evaluation of Lemoine *et al.* (1996). Our value is in disagreement with the EUV measurements of Kimble *et al.* (1993) using the HUT, $N(\text{H I})=1.7 \times 10^{18} \text{ cm}^{-2}$, Green *et al.* (1990) using a rocket-borne spectrograph, $N(\text{H I})=1.6 \times 10^{18} \text{ cm}^{-2}$, Holberg *et al.* (1990), $N(\text{H I})=1.0 \times 10^{18} \text{ cm}^{-2}$, Bruhweiler & Kondo (1982) using NI and the relationship between $N(\text{N I})$ and $N(\text{H I})$, $N(\text{H I})=0.8 \times 10^{18} \text{ cm}^{-2}$. Our estimate is however in agreement within the error bars with those of Jelinsky *et al.* (1988) and Paerels & Heise (1989). Moreover, it is in good agreement with the recent EUV measurements of Dupuis *et al.* (1995) and Lanz *et al.* (1996), $N(\text{H I})=2.1 \times 10^{18} \text{ cm}^{-2}$, that use more modern white dwarf atmosphere models.

The fit of the Lyman limit by Kimble *et al.* (1993), Holberg *et al.* (1990) comes through the modeling of the atmosphere of G191-B2B with homogeneous atmosphere models. Their analysis might thus be questioned in view of the recent detection of non-negligible amounts of highly ionized metallic species (Nv, Fev, Siiv) in this photosphere (see Vidal-Madjar *et al.* 1994), although trace of metallic species are not believed to contribute significantly to the absorption over 500\AA . We find a total NI column density in perfect agreement with that found by Bruhweiler & Kondo (1982), and the difference between the $N(\text{H I})$ values is directly related to the difference found in the relationship $N(\text{N I})-N(\text{H I})$ between our observations and that of Ferlet (1981) on different lines of sight.

5. Discussion

Our results lead us to the following statement: either the D/H ratio is constant in the local ISM, its value is $1.12 \pm 0.08 \times 10^{-5}$, and the estimate made in the direction of Capella by L95 is incorrect; or, the D/H ratio does vary in the local ISM. If this latter hypothesis is verified, we need to check whether the D/H ratio can vary within a same cloud, the LIC, which is common to both the Capella and the G191-B2B line of sight, or whether it varies on larger spatial scales, from cloud to cloud.

It thus seems reasonable to re-analyze the evaluation made by L93, L95 with the same techniques that we used to derive the D/H ratio toward G191-B2B. This we do now.

5.1. Capella revisited

The Capella high resolution GHRs Echelle-A data are of high quality, with a spectral resolution $\Delta\lambda = 3.5\text{km.s}^{-1}$, and a signal-to-noise ratio $S/N \simeq 40$ at the interstellar Lyman α line continuum. For this star, the accuracy on the estimate of the D/H ratio is limited by the ability to reconstruct the Lyman α stellar emission profile of Capella, all the more since it is composed of the combined profiles of the two cool stars of the binary system. L95 circumvented this problem by observing Capella at two different phases, and were thus able to reconstruct, at least partly, both stellar continua.

As our paper is not dedicated to the study of this line of sight, we only summarize our study of the Capella data set, and jump to the conclusions. In order to model the stellar continuum, we used two different approaches, in the same spirit as Section 3.1: in the first approach, we used the stellar continuum produced by L95, and in the other, we constructed a stellar profile in a very naive manner, by interpolating the far wings of the emission profile with a 7th degree polynomial. This latter polynomial would then be further corrected in the core by a 4th order polynomial. In all our fits, we found that the continuum found by L95 was the most appropriate in terms of χ^2 statistics, and hence we will not refer to this 7th \times 4th order polynomial continuum anymore. L95 detected only one component on the line of sight, from the analysis of the narrow metal lines of MgII and FeII. We followed these authors and proceeded to the profile fitting with only one component on the line of sight. A first analysis gave results in agreement with their work, although we find $N(\text{D I}) = 2.6 \pm 0.1 \times 10^{13}\text{cm}^{-2}$, in disagreement with the original estimate of L95, $N(\text{D I}) = 2.85 \pm 0.1 \times 10^{13}\text{cm}^{-2}$. It probably results from a slight mismatch in the radial velocity of the D I and H I lines, with a shift of 0.3km.s^{-1} for the D I line away from the expected position, to be compared with an error on the radial velocity of only $\pm 0.1\text{km.s}^{-1}$. Whereas our D I and H I lines automatically have the same radial velocity, L95 did not link the radial velocities of the D I and of the H I absorbers. Nevertheless, this seems to point to the existence of another component, that would perturb the H I line but not the D I line.

Wood & Linsky (1998) did mention that such a perturbation should be present, and due to the absorption by the hydrogen atoms in the Earth geocorona, which, at the time of the observations, was located in velocity space a -22km.s^{-1} . This absorption is shown in Fig. 17. When we attempt a fit with a two component solution, we obtain a better χ^2 with a $\Delta\chi^2 \sim 100$, a dramatic improvement indeed. In this two component solution, we left both components entirely free. Interestingly enough, we obtained two kinds of solution: in both cases, the main component was extremely similar to the single component (LIC) of L95; in one case, however, the extra absorption was caused by a cold, *i.e.* small broadening component, located around

Table 8. Physical parameters evaluated on the line of sight to Capella from Cycle 1 GHRs archival data. We assumed the presence of three components on the line of sight, which represents a gain $\Delta\chi^2 \sim 100$ in χ^2 over the one cloud solution. The additional components are noted “Hot” and “Geo” and were left as entirely free in the profile fitting. The data are here normalized with the stellar continuum reconstructed by L95 and corrected by a 4th order polynomial.

Stellar continuum	Linsky $\times 4^{\text{th}}$ order polynomial
$\chi^2 / 198$	0.79
$N(\text{H I})_{\text{LIC}} (\text{cm}^{-2})$	1.72×10^{18}
$N(\text{D I})_{\text{LIC}} (\text{cm}^{-2})$	2.69×10^{13}
$(\text{D/H})_{\text{LIC}} (\times 10^5)$	1.56
$V_{\text{LIC}} (\text{km.s}^{-1})$	23.05
$T_{\text{LIC}} (\text{K})$	6053.
$\sigma_{\text{LIC}} (\text{km.s}^{-1})$	2.96
$N(\text{H I})_{\text{Geo}} (\text{cm}^{-2})$	1.74×10^{12}
$V_{\text{Geo}} (\text{km.s}^{-1})$	-22.00
$T_{\text{Geo}} (\text{K})$	2113.
$N(\text{H I})_{\text{Hot}} (\text{cm}^{-2})$	4.00×10^{14}
$V_{\text{Hot}} (\text{km.s}^{-1})$	+21.50
$T_{\text{Hot}} (\text{K})$	26667.

$\sim -20\text{km.s}^{-1}$; in a second case, slightly favored over the previous one, in terms of χ^2 , we obtained a hot component, with $T \sim 30000\text{K}$, located around $\sim +20\text{km.s}^{-1}$. Our profile fitting algorithm indeed works by random minimization, and can therefore find different degenerate solutions for a same dataset. Since both of these extra components fall at smaller radial velocities than the LIC, they produce a shift of the H I absorption, and reconcile the overall radial velocities of both H I and D I lines.

Since we know that the geocorona has to be present, we performed a three cloud solution, with all parameters free. We found, in that case, both previous extra components, *i.e.* one hot, located around $\sim +20\text{km.s}^{-1}$, and one cold component, located at -22.0km.s^{-1} ! The final characteristics are given in Table 8, and the fit is shown in Fig. 17. The geocorona found here is entirely consistent with the actual geocorona, in terms of H I column density, velocity, and temperature.

The “Hot” component falls at an heliocentric velocity of order $21.5 \pm 1.5\text{km.s}^{-1}$, with an effective broadening temperature $T \sim 27000_{-4000}^{+18000}\text{K}$. Its characteristics are well defined, even though it seems to be constrained from one side only of the H I line, probably because its presence is felt, in these high quality data, over nearly 1\AA . This component may be identified with a cloud interface, as first detected by Bertin *et al.* (1995) toward Sirius A, or with a “hydrogen wall” as proposed and discussed by Linsky & Wood (1996), Piskunov *et al.* (1997), Dring *et al.* (1997), and Wood & Linsky (1998).

Its slightly shifted value redward of the LIC is compatible with the “hydrogen wall” concept since it assumes

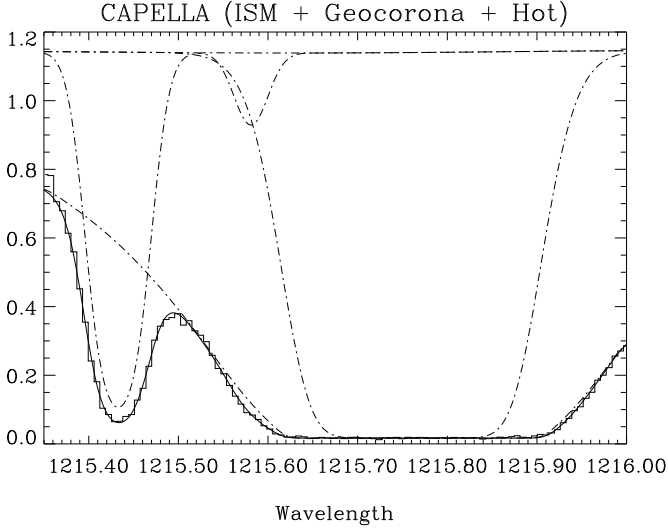


Fig. 17. The best fit obtained with three components assumed along the Capella line of sight. The stellar continuum assumed here is the one reconstructed by L95 and corrected by a 4th order polynomial. The two additional components are imposed by the data points near 1215.6Å which cannot be fitted by any simpler “one cloud” solution. The weak additional component needed at -22km.s⁻¹ is at the velocity shift of the earth geocorona but cannot alone fit correctly the 1215.6Å feature. A third “hot” component is also needed (see text).

a slowing down of the ISM hydrogen atoms when interacting with the stellar wind itself. If correct, this seems to indicate that the LIC extends out to Capella, and that it is quite homogeneous in that direction, since the average volume density toward Capella is then very similar to the one observed within the solar system.

We expect this component to be entirely compatible with our observations of G191-B2B as it would fall in between components 2 and 3, in a region where the H I Lyman α line is completely saturated.

In summary, our estimate of the D/H ratio toward Capella is:

$$(D/H)_{\text{Capella}} = 1.56 \pm 0.1 \times 10^{-5},$$

in perfect agreement with the original estimate. From these data alone we also estimated the other characteristics of the LIC independently and found that its temperature should be $T_{\text{LIC}} = 6750 \pm 250$ K if the microturbulence of the LIC is properly constrained by the other spectral lines as given in L95.

As a conclusion, we thus confirm the estimate of L95 of the D/H ratio within the LIC, $(D/H) = 1.6 \pm 0.1 \times 10^{-5}$, but seem to evaluate a slightly cooler LIC temperature, more compatible with the G191-B2B evaluation. The LIC D/H estimate made toward Capella is thus marginally compatible with the evaluation made within the LIC in the direction of G191-B2B, and in any case clearly incompat-

ible with the estimate of the average D/H ratio on this latter line of sight.

The D/H ratio thus has to vary within the local ISM.

6. Conclusion

The outcome of our Cycle 5 observations of the white dwarf G191-B2B performed with the GHRS of HST, aiming to derive “bona fide” value(s) of the D abundance in the local interstellar medium is the following : Overall 8 absorption complexes of the elements Si II, Si III, N I, O I, and, of course, H I and D I, were observed at high resolution (Echelle-A grating), and analyzed simultaneously using a new profile fitting procedure. We extract an accurate description of the cloud structure along the line of sight, which consists of three absorbing clouds, separated by ~ 5 km.s⁻¹. The third absorber, to be understood in terms of increasing radial velocity, at a heliocentric velocity $V = 20.4 \pm 0.8$ km.s⁻¹, is identified with the Local Interstellar Cloud in which the Sun is embedded. The network of constraints on these clouds, that results from the profile fitting of the different interstellar lines, is such that we can derive the temperature and the turbulent velocities in the different interstellar components, as well as the column densities of the various observed species. Our new set of high quality data is consistent with the Lemoine *et al.* (1996) evaluation of the total H I column density towards G191-B2B, *i.e.* $N(\text{H I}) = 2.4 \pm 0.1 \times 10^{18}$ cm⁻².

We derive an average D/H ratio over the three absorbing clouds $N(\text{D I})_{\text{total}}/N(\text{H I})_{\text{total}} = 1.12 \pm 0.08 \times 10^{-5}$. The Local Interstellar Cloud, detected here toward G191-B2B, has also been detected on the line of sight toward Capella, and its D/H ratio has been measured by Linsky *et al.* (1993, 1995): $(D/H)_{\text{Capella}} = 1.6 \pm 0.1 \times 10^{-5}$. We have re-analyzed the data of L95 toward Capella, and confirm their estimate of the D/H ratio, as we find: $(D/H)_{\text{Capella}} = 1.56 \pm 0.1 \times 10^{-5}$. We find that the D/H ratio in this Local Interstellar Cloud, on the line of sight to G191-B2B can be made consistent with the Capella value. However, this comes at the expense of a much smaller average D/H ratio in components 1 and 2, of order 0.9×10^{-5} , in such a way that the D/H ratio averaged over all three components remains at the above value 1.12×10^{-5} .

Therefore, we conclude that the D/H ratio indeed varies in the local ISM over a few parsecs and at least from interstellar cloud to interstellar cloud. Although we do not detect variations of the (D/H) ratio within the Local Interstellar Cloud itself, such variations may become clear as more data are analyzed. Here, we note that both clouds 1 and 2 are more like H II regions while the Local Interstellar Cloud could be identified with an H I region; this ionization difference might point to the cause of this (D/H) variation.

These large variations of the ISM D/H ratio in so small scales cannot be due to any nuclear processes (spallation processes induced by cosmic rays or by huge gamma ray

fluxes) occurring in that medium. We mention here two other possibilities:

(i)- given the fact that the column density is only of the order of a few 10^{18}cm^{-2} the lowest D/H value could be due to the admixture of a comparable amount of D-free, pure H remnant of a material within the considered cloud.

(ii)- these low D components could be the remnants of semi-thermalized blobs of material coming from the outer layers released during the planetary nebula phase of evolution.

As a rule, it is much easier to deplete than to create deuterium. In this case, just as in the two possibilities mentioned above, the lowest ISM D/H values would be due to a secondary effect, and the highest value would be more representative of an actual ISM D/H ratio. However, nothing precludes the Capella value from being itself affected by such a secondary effect. Moreover, we point out that the deuterium abundance may be locally enhanced (or depleted) when the radiation flux is anisotropic, as the radiation pressure acts differently on HI and DI (Vidal-Madjar *et al.* 1978; Bruston *et al.* 1981).

To sum up the consequences of the present investigation, the question concerning the existence or not of variations of the D/H ratio in the ISM has now an answer : variations do exist within the local ISM of order $\approx 30\% - 50\%$ within a few parsecs, and/or within a given cloud, the Local Interstellar Cloud. To be more precise, our observations show that the average (D/H) ratio on the line of sight to G191-B2B (averaged over three interstellar components), is significantly different from the (D/H) ratio measured toward Capella. Although the Local Interstellar Cloud is common to both lines of sight, we do not find conclusive evidence for variation of the (D/H) ratio in this particular component.

The comparisons between the theoretical predictions of standard Big-Bang nucleosynthesis combined with those coming from the recent models of chemical evolution of deuterium and the measured D/H ratios in the different components of these lines of sight appear to be more complex to establish. Forthcoming analyses will have now to take into account these D/H variations and should discuss more thoroughly some of the possibilities envisaged above.

We therefore look forward to: (i) further observations of the interstellar deuterium abundance on other nearby lines of sight. In this respect, white dwarfs seem to constitute a highly reliable way of achieving a precise measurement of the deuterium abundance in the nearby interstellar medium. In effect, white dwarfs present neither the complex stellar continuum of cool stars, nor the complex interstellar velocity structure that arises towards more distant hot stars. (ii) Measurements of the D/H ratio in spiral arms of the Galaxy distinct from ours, or in low-redshift systems, performed in the framework of the FUSE-LYMAN mission.

Acknowledgements. It is a pleasure to thank S. Burles and D. York for many stimulating discussions. We also thank J. Linsky and J. Wampler for a careful reading of the manuscript, L. BenJaffel and O. Puyoo for ionization calculations, as well as S. Dreizler for the calculation of theoretical line profiles. We are also indebted to the whole HST Team and in particular to A. Berman who has always been extremely helpful in the preparation of the observations. Work on HST observations in Kiel is supported by grants from the Deutsches Zentrum für Luft- und Raumfahrt (DLR).

References

- Audouze, J., and Tinsley, B.M.: 1976, *ARAA* **14**, 43.
 Allen, M. M., Jenkins, E. B., Snow, T. P.: 1992, *ApJS* **83**, 261.
 Bertin, P., Vidal-Madjar, A., Lallement, R., Ferlet, R., Lemoine, M.: 1995, *AA* **302**, 889.
 Bruhweiler, F. C., Kondo, Y.: 1982, *ApJ* **259**, 232
 Boesgaard, A.M., and Steigman, G.: 1985, *ARAA* **23**, 319.
 Bruston, P., Audouze, J., Vidal-Madjar, A., and Laurent, C.: 1981, *ApJ* **243**, 161.
 Burles, S., Tyler, D.: 1998a, submitted to *ApJ*, [astro-ph/9812108](#)
 Burles, S., Tyler, D.: 1998b, submitted to *ApJ*, [astro-ph/9812109](#)
 Burles, S., Tytler, D.: 1998c, Proceedings of the Second Oak Ridge Symposium on Atomic & Nuclear Astrophysics, ed. A. Mezzacappa (Institute of Physics, Bristol), to appear, [astro-ph/9803071](#)
 Carswell, R.F., Rauch, M., Weymann, R.J., Cooke, A.J., Webb, J.K.: 1994, *MNRAS* **268**, L1.
 Dreizler, S.: private communication
 Dring, A., Linsky, J., Murthy, J., Henry, R.C., Moos, W., Vidal-Madjar, A., Audouze, J., and Landsman, W.: 1997, *ApJ* **488**, 760.
 Duncan, D. : 1992, *Hubble Space Telescope Goddard High Resolution Spectrograph Instrument Handbook*, version 3.0, STScI
 Dupin, O., and Gry, C.: 1998, *AA* in press.
 Dupuis, J., Vennes, S., Bowyer, S., Pradhan, A.K., Thejll, P.: 1995, *ApJ* **455**, 574
 Epstein, R.I., Lattimer, J.M., Schramm, D.N.: 1976, *Nature* **263**, 198
 Ferlet, R.: 1981, *AA* **98**, L1.
 Finley, D.S., Koester, D., Basri, G.: 1997, *ApJ* **488**, 375.
 Fitzpatrick, E.L., Spitzer, L.: 1994, *ApJ* **427**, 232.
 Fitzpatrick, E.L., Spitzer, L.: 1997, *ApJ* **475**, 623.
 Geiss, J., and Reeves, H.: 1972, *AA* **18**, 126.
 Green, J., Jelinsky, P., Bowyer, S.: 1990, *ApJ* **359**, 499
 Grevesse, N., and Noels, A.: 1993, *Origin and Evolution of the Elements*, *CUP*, 15.
 Gry, C. and Dupin, O.: 1998, in *Proceedings of the IAU Colloquium N° 166*, "Local Bubble and Beyond", eds. D. Breitschwerdt, M.J. Freyberg, J. Trumper, Lecture Notes in Physics, **506**, 161.
 Gry, C., Lemonon, L., Vidal-Madjar, A., Lemoine, M., Ferlet, R.: 1995, *AA* **302**, 497.
 Holberg, J.: 1990, in *Extreme Ultraviolet Astronomy*, eds. R. F. Malina, S. Bowyer
 Jelinsky, P., Bowyer, S., Basri, G.: 1988, in *A Decade of UV Astronomy with IUE - A Celebratory Symposium*, **2**, 235

- Jenkins, E.B., Wallerstein, G.: 1996, ApJ **462**, 758.
- Kimble, R.A., Davidsen, A.F., Blair, W.P., Bowers, C.W., Van Dyke Dixon, W., Durrance, S.T., Feldman, P.D., Ferguson, H.C., Henry, R.C., Kriss, G.A., Kruk, J.W., Long, K.S., Moos, H.W., Vancura, O.: 1993, ApJ **404**, 663
- Lallement, R., Bertin, P.: 1992 AA **266**, 479
- Lanz, T., Barstow, M.A., Hubeny, I., Holberg, J.B.: 1996, ApJ **473**, L1089
- Laurent, C., Vidal-Madjar, A., and York, D.G.: 1979, ApJ **229**, 923.
- Lemoine, M., Vidal-Madjar, A., Bertin, P., Ferlet, R., Gry, C., Lallement, R.: 1996, AA **308**, 601.
- Linsky, J. L., Brown, A., Gayley, K., Diplas, A., Savage, B.D., Ayres, T.R., Landsman, W., Shore, S. W., Heap, S. R.: 1993, ApJ **402**, 694.
- Linsky, J., Diplas, A., Wood, B.E., Brown, A., Ayres, T.R., Savage, B.D.: 1995, ApJ **451**, 335.
- Linsky, J., and Wood, B.E.: 1996, ApJ **463**, 254.
- Meyer, D. M., Jura, M., Cardelli, J. A.: 1998a, ApJ **493**, 222
- Meyer, D. M., Cardelli, J. A., Sofia, U. J.: 1998b, *preprint astro-ph/9710162*.
- Murthy, J., Henry, R. C., Moos, H. W., Landsmann, W. B., Linsky, J. L., Vidal-Madjar, A., Gry, C.: 1987, ApJ **315**, 675
- Murthy, J., Henry, R. C., Moos, H. W., Landsmann, W. B., Vidal-Madjar, A., Linsky, J. L., Gry, C.: 1990, ApJ **356**, 223
- Olive, K., Schramm, D., Steigman, G., and Walker, T.: 1990, Phys. Lett. **236B**, 454.
- Paerels, B. S., Heise, J.: 1989, ApJ **339**, 1000
- Piskunov, N., Wood, B.E., Linsky, J. L., Dempsey, R.C., and Ayres, T.R.: 1997, ApJ **474**, 315.
- Prantzos, N.: 1996, AA **310**, 106.
- Puyoo, O., and BenJaffel, L.: 1998, in *Proceedings of the IAU Colloquium N° 166*, "Local Bubble and Beyond", eds. D. Breitschwerdt, M.J. Freyberg, J. Trumper, Lecture Notes in Physics, **506**, 29.
- Reeves, H., Audouze, J., Fowler, W.A., Schramm, D.N.: 1973, ApJ **179**, 909
- Reid, N., Wegner, G.: 1988, ApJ **335**, 953
- Rogerson, J., and York, D.: 1973, ApJ **186**, L95.
- Savage, B.D., and Sembach, K.R.: 1996, ARAA **34**, 279.
- Scully, S.T., Cassé, M., Olive, K.A., Vangioni-Flam, E.: 1997, ApJ **476**, 521.
- Songaila, A., Cowie, L.L., Hogan, C.J., and Rugers, M.: 1994, *Nature* **368**, 599.
- Spitzer, L., Fitzpatrick, E.L.: 1993, ApJ **409**, 299.
- Spitzer, L., Fitzpatrick, E.L.: 1995, ApJ **445**, 196.
- Steigman, G., Schramm, D.N., Gunn, J.: 1977, Phys. Lett. **66B**, 202
- Tytler, D., Fan, X.-M., Burles, S.: 1996, *Nature* **381**, 207
- Vangioni-Flam, E., Cassé, M.: 1995, ApJ **441**, 471.
- Vangioni-Flam, E., Olive, K.A., Prantzos, N.: 1994, ApJ **427**, 618.
- Vauclair, G., Schmidt, H., Koester, D., Allard, N.F.: 1997, AA **325**, 1055.
- Vidal-Madjar, A., Laurent, C., Bruston, P., and Audouze, J.: 1978, ApJ **223**, 589.
- Vidal-Madjar, A., and Gry, C.: 1984, AA **138**, 285.
- Vidal-Madjar, A., Ferlet, R., Gry, C., Lallement, R.: 1986, AA **155**, 407
- Vidal-Madjar, A., Allard, N., Koester, D., Lemoine, M., Ferlet, R., Bertin, P., Lallement, R., Vauclair, G.: 1994, AA **287**, 175
- Webb, J.K., Carswell, R.F., Lanzetta, K.M., Ferlet, R., Lemoine, M., Vidal-Madjar, A., and Bowen, D.V.: 1997, *Nature* **388**, 250.
- Welty, D.E., Lauroesch, J.T., Blades, J.C., Hobbs, L.M., York, D.G.: 1997, ApJ **489**, 672
- Wolff, B., Koester, D., Dreizler, S., Haas, S. 1998, AA **329**, 1045.
- Wood, B.E., and Linsky, J.: 1997, ApJ **474**, L39.
- Wood, B.E., and Linsky, J.: 1998, ApJ **492**, 788.
- York, D.G.: 1983, ApJ **264**, 172.
- York, D.G., Spitzer, L., Bohlin, R.C., Hill, J., Jenkins, E.B., Savage, B.D., Snow, T.P.: 1983, ApJ **266**, L55.